



HAL
open science

Transformation of Ni-containing birnessite to tectomanganate: Influence and fate of weakly bound Ni(II) species

Zhongkuan Wu, Bruno Lanson, Xionghan Feng, Hui Yin, Zhangjie Qin, Xiaoming Wang, Wenfeng Tan, Zhongjun Chen, Wen Wen, Fan Liu

► To cite this version:

Zhongkuan Wu, Bruno Lanson, Xionghan Feng, Hui Yin, Zhangjie Qin, et al.. Transformation of Ni-containing birnessite to tectomanganate: Influence and fate of weakly bound Ni(II) species. *Geochimica et Cosmochimica Acta*, 2020, 271, pp.96-115. 10.1016/j.gca.2019.12.023 . insu-02984573

HAL Id: insu-02984573

<https://insu.hal.science/insu-02984573>

Submitted on 25 Nov 2020

HAL is a multi-disciplinary open access archive for the deposit and dissemination of scientific research documents, whether they are published or not. The documents may come from teaching and research institutions in France or abroad, or from public or private research centers.

L'archive ouverte pluridisciplinaire **HAL**, est destinée au dépôt et à la diffusion de documents scientifiques de niveau recherche, publiés ou non, émanant des établissements d'enseignement et de recherche français ou étrangers, des laboratoires publics ou privés.

1 **Transformation of Ni-containing birnessite to**
2 **tectomanganate:**
3 **Influence and fate of weakly bound Ni(II) species**

4
5 Zhongkuan Wu^{a,b}, Bruno Lanson^{b,*}, Xionghan Feng^a, Hui Yin^a, Zhangjie Qin^a,
6 Xiaoming Wang^a, Wenfeng Tan^a, Zhongjun Chen^c, Wen Wen^d, Fan Liu^{a,*}

7
8 ^a *Key Laboratory of Arable Land Conservation (Middle and Lower Reaches of*
9 *Yangtse River) Ministry of Agriculture, College of Resources and Environment,*
10 *Huazhong Agricultural University, Wuhan 430070, China*

11 ^b *Univ. Grenoble Alpes, Univ. Savoie Mont Blanc, CNRS, IRD, IFSTTAR,*
12 *ISTerre, F-38000 Grenoble, France*

13 ^c *Beijing Synchrotron Radiation Facility, Institute of High Energy Physics,*
14 *Chinese Academy of Sciences, Beijing 100039, China*

15 ^d *Shanghai Synchrotron Radiation Facility, Shanghai Advanced Research*
16 *Institute Chinese Academy of Sciences, Shanghai 201204, China*

17
18 * Corresponding author: bruno.lanson@univ-grenoble-alpes.fr;
19 liufan@mail.hzau.edu.cn

20

21 **Abstract**

22 The geochemical behavior of nickel, an essential trace metal element, strongly
23 depends on its interactions with Mn oxides. Interactions between the phylломanganate
24 birnessite and sorbed or structurally incorporated Ni have been extensively
25 documented together with the fate of Ni along the transformation of these layered
26 species to tunnel Mn oxides (tectomanganates). By contrast, interactions of
27 phylломanganates with weakly bound Ni species (hydrated Ni, Ni (hydr)oxides), that
28 possibly prevail in natural Ni-rich (>10% NiO) manganates received little attention
29 and the influence of these Ni species on the phylломanganate-to-tectomanganate
30 transformation remains essentially unknown. Within this framework, a set of
31 phylломanganate precursors with contrasting contents of Ni were prepared and
32 subjected to a reflux process mimicking the natural
33 phylломanganate-to-tectomanganate conversion. Layered precursors and reflux
34 products were characterized with a combination of diffractometric, spectroscopic,
35 thermal, and chemical methods. Ni is essentially present as hydrated Ni(II) and Ni(II)
36 (hydr)oxides in layered precursors with no detectable Ni sorbed at layer vacancy sites
37 or structurally incorporated. Despite the high content (~1/3) of Jahn-Teller distorted
38 Mn(III) octahedra in these layered precursors, which is known to be favorable to their
39 conversion to tectomanganates, polymerization of Ni(OH)₂ in phylломanganate
40 interlayers is kinetically favored during reflux process. Asbolane, a phylломanganate
41 with an incomplete – island-like – octahedral layer of metal (hydr)oxides, is thus
42 formed rather than todorokite, a common tectomanganate with a uniform 3×3 tunnel
43 structure. A nitric acid treatment, aiming at the dissolution of the island-like interlayer
44 Ni(OH)₂ layer, allows an easy and unambiguous differentiation between asbolane and
45 todorokite, which is unaffected by the treatment. Both compounds exhibit indeed
46 similar periodicities and can be confused when using X-ray diffraction, despite
47 contrasting intensity ratios. Ni(OH)₂ polymerization hampers the formation of
48 tectomanganates and likely contributes to the prevalence of phylломanganates over

49 tectomanganates in natural environments. Most Ni is retained during the reflux
50 process, part of Ni (~20%) being likely structurally incorporated in the reaction
51 products, thus enhancing the sequestration of Ni in Mn oxides.

52 *Keywords:* nickel; busserite; asbolane; todorokite; Mn oxides

53

1. INTRODUCTION

54

55

56 Phylломanganates and tectomanganates are the two mineral families accounting
57 for most of Mn oxides found in terrestrial and aquatic environments (Post, 1999;
58 Peacock and Sherman, 2007a). In the former, edge-sharing MnO_6 octahedra form
59 layers whose symmetry depends on the abundance and distribution of Mn(III)
60 octahedra, whereas in the latter, chains of edge-sharing Mn(IV)O_6 octahedra form the
61 walls or floor/ceiling of tunnels. Birnessite is, together with its disordered structural
62 analogue vernadite, the most common phylломanganate and consists of a MnO_2 layer,
63 whose layer charge deficit is compensated for by the presence of cations sorbed at
64 layer vacancy sites or present as interlayer hydrated species (7.0-7.2 Å layer-to-layer
65 distance). Heterovalent Mn cations and/or foreign transition metal cations can be
66 hosted in both families, either structurally substituted for Mn(IV) or as charge
67 compensating cations located in phylломanganate interlayers or in tectomanganate
68 tunnels (Post, 1999). The occurrence of natural phylломanganates as micro- to
69 nano-sized cryptocrystalline minerals usually enhances their surface reactivity that
70 originates from their high negative layer charge and from the coexistence of
71 heterovalent Mn cations in these structures. As the result, natural phylломanganates
72 are highly reactive with respect to both organic (Remucal and Ginder-Vogel, 2014)
73 and inorganic compounds. Specifically, natural phylломanganates are readily
74 associated with transition metals such as Co, Cu, Zn, or Ni (Chukhrov, 1982;
75 Manceau et al., 1987, 1992a,b, 2002, 2007a,b, 2014; Marcus et al., 2004; Bodeř et al.,
76 2007; Peacock and Sherman, 2007a; Lanson et al., 2008; Spinks et al., 2017;
77 Zawadzki et al., 2018), rare earth (Kasten et al., 1998; Ohta and Kawabe, 2001;
78 Ohnuki et al., 2015; Zawadzki et al., 2018), and radioactive elements (Duff et al.,
79 1999; Post, 1999).

80 In an effort to disentangle the mobility, (bio)availability, and fate of these
81 elements in different geological settings, structural interactions of phylломanganates
82 with such foreign elements, and more especially with transition metals, have thus

83 attracted the attention of the scientific community over the last few decades (Manceau
84 et al., 1997, 2002, 2014; Ohta and Kawabe, 2001; Lanson et al., 2002a; Marcus et al.,
85 2004; Toner et al., 2006; Peacock and Sherman, 2007a,b; Peacock, 2009; Peña et al.,
86 2010; Roque-Rosell et al., 2010; Sherman and Peacock, 2010; Yin et al., 2011a,b;
87 Kwon et al., 2013; Yu et al., 2013; Burlet and Vanbrabant, 2015; Simanova et al.,
88 2015). In most studies, foreign elements were structurally substituted for Mn(IV) in
89 the MnO₆ octahedra or sorbed as inner-sphere complexes either at vacant layer sites
90 and/or at particle edges (Manceau et al., 1997; Yin et al., 2011a, 2015; Yu et al., 2013;
91 Ohnuki et al., 2015; Simanova and Pena, 2015; Qin et al., 2018). Similar to other
92 transition metals, presence of Ni(II) forming inner-sphere complexes species at
93 vacancy or edge sites and/or structurally incorporated in phyllosmanganate layers has
94 been extensively documented (Manceau et al., 2002, 2007a,b; Peacock and Sherman,
95 2007a,b; Grangeon et al., 2008; Peña et al., 2010; Yin et al., 2012, 2014; Kwon et al.,
96 2013; Simanova et al., 2015). Under low pH conditions, Ni(II) occurs mainly as
97 triple- or double-corner sharing (TCS and DCS, respectively) inner-sphere complex
98 above/below vacancy or at edge sites of the phyllosmanganate layers (Peacock and
99 Sherman, 2007b; Grangeon et al., 2008; Peacock, 2009; Peña et al., 2010; Simanova
100 et al., 2015). Migration from TCS/DCS sites to octahedral layer sites is favored by
101 increasing contact time and increasing pH (Peacock, 2009), this structural
102 incorporation within the octahedral MnO₂ layer being reversible (Peacock, 2009; Peña
103 et al., 2010) and essentially restricted to low Ni contents (Manceau et al., 2002; Bodeř
104 et al., 2007; Peacock and Sherman, 2007a,b; Kwon et al., 2013; Simanova et al., 2015;
105 Atkins et al., 2016), consistent with natural occurrences (Manceau et al., 2002,
106 2007a,b; Bodeř et al., 2007; Peacock and Sherman, 2007a).

107 In addition, hydrated Ni(II) or Ni forming outer-sphere complexes (Turner and
108 Buseck, 1981; Peacock and Sherman, 2007a) and Ni(II) (hydr)oxides (Chukhrov et al.,
109 1987; Manceau et al., 1987, 1992a,b) may also be associated with Mn oxides. Despite
110 their widespread natural occurrences for high Ni contents (NiO ~10-20 wt.%, – Llorca,
111 1988; Roque-Rosell et al., 2010; Ploquin et al., 2018), these weaker associations have
112 received little attention compared to structurally incorporated Ni or to Ni inner-sphere

113 complexes. The presence of hydrated Ni(II) species in phylломanganate interlayers
114 leads to the presence of two planes of interlayer water molecules, thus increasing the
115 layer-to-layer distance from ~ 7.2 Å (birnessite or vernadite) to ~ 9.6 - 10.2 Å (buserite –
116 Burns et al., 1983; Chukhrov et al., 1987; Golden et al., 1987; Manceau et al., 1997,
117 2014; Bodeř et al., 2007; Wegorzewski et al., 2015). Such increased hydration of
118 Ni-rich phylломanganates has for example been reported by Manceau et al. (2007b).
119 The presence of hydrated Ni(II) in phylломanganate interlayers has been described
120 also as favorable to the transformation of phylломanganate to tectomanganates upon
121 hydrothermal treatment (Ching et al., 1999; Luo et al., 1999; Onda et al., 2007),
122 similar to Mg(II) (Golden et al., 1986, 1987). In addition, Ni(II) (hydr)oxides may
123 polymerize in phylломanganate interlayers either as a complete or as an incomplete
124 brucite-like octahedral layer, leading to litiophorite- or asbolane-like species,
125 respectively, both having a layer-to-layer distance of 9.4 - 9.8 Å (Chukhrov et al., 1987;
126 Manceau et al., 1987, 1992a,b; Feng et al., 2001).

127 The present article thus focuses on the association of these weakly bound Ni(II)
128 species with phylломanganates. Synthetic samples with contrasting Ni contents were
129 prepared and characterized by X-ray diffraction, Fourier transform infrared
130 spectroscopy, thermogravimetric analysis, X-ray photoelectron spectroscopy,
131 extended X-ray absorption fine structure spectroscopy (Mn and Ni K-edges). In
132 addition, phylломanganate samples were hydrothermally treated and reaction products
133 characterized to investigate the effect of Ni on the
134 phylломanganate-to-tectomanganate transformation (Golden et al., 1986; Shen et al.,
135 1993; Feng et al., 2004, 2010; Atkins et al., 2014; Grangeon et al., 2014, 2015; Zhao
136 et al., 2015) and the fate of weakly associated Ni(II) species during this
137 transformation. The negative impact of Ni, when present at high content, on this
138 transformation is contrasted with that of Co. Buserite-, litiophorite-, and asbolane-like
139 phylломanganates all have interplanar periodicities similar to those of todorokite, a
140 common tectomanganate with a uniform 3×3 tunnel structure (Post and Bish, 1988),
141 however, leading to their frequent confusion (Burns et al., 1983). Special care was
142 thus paid to allow differentiating these species using nitric acid treatment (Wu et al.,

143 2019), Fourier transform infrared spectroscopy and anomalous X-ray diffraction. An
144 optimum procedure allowing this differentiation is proposed.

146 2. MATERIALS AND METHODS

148 2.1. Synthesis of layered precursors and reflux products

149
150 Both initial layered precursors and reflux products described in the present study
151 were prepared as in our previous work on their Co analogues (Wu et al., 2019).
152 Briefly, layered precursors were prepared after Feng et al. (2004) and Song et al.
153 (2010) by adding a concentrated NaOH solution into a Ni(II) + Mn(II) solution,
154 prepared from their chloride salts. The resulting solution was then mixed and bubbled
155 with oxygen gas for 5 h. Resulting black precipitates were washed and one half was
156 dried for subsequent analyses. Initial Ni / (Ni + Mn) ratios were 0.00, 0.01, 0.05, 0.10,
157 0.15, and 0.20. Accordingly, initial layered samples were named Bir, NiB1, NiB5,
158 NiB10, NiB15 and NiB20, and those Ni-containing samples are collectively referred
159 to as NiB. The other half of the precipitates was used to prepare todorokite through a
160 reflux process following the protocol of Feng et al. (2004). Wet precipitates were thus
161 exchanged with Mg^{2+} , rinsed, re-suspended in deionized water, and finally refluxed at
162 100 °C for 24 h. Reflux products were finally filtered, washed, and dried.
163 Transformation products of Bir, NiB1, NiB5, NiB10, NiB15 and NiB20 are named
164 Tod, NiT1, NiT5, NiT10, NiT15 and NiT20, respectively; they are collectively
165 referred to as NiT except for Tod. Both layered precursors and reflux products were
166 dried at 60 °C for three days and ground into fine powders.

168 2.2. Characterization of layered precursors and reflux products

169
170 The elemental composition of all samples was determined in triplicate using
171 atomic absorption spectrometry (Varian AAS 240FS) from 0.1000 g of sample

172 dissolved in 25 mL solution of 0.25 mol L⁻¹ NH₂OH·HCl and 5 mL of 1 mol L⁻¹
173 H₂SO₄. In addition, the specific surface area (SSA) of the reflux products was
174 determined with the Brunauer–Emmett–Teller (BET) method and a standard
175 adsorption analyzer (Quantachrome Autosorb-1, JEDL-6390/LV). Finally, a
176 non-reducing nitric acid treatment (Wu et al., 2019) was performed to differentiate
177 tectomanganates (todorokite) from phyllomanganates (buserite-, lithiophorite-, or
178 asbolane-like phases – Wu et al., 2019). Briefly, 0.1 g sample was put in 250 mL of a
179 1 M HNO₃ solution with soft stirring at ambient temperature (20 °C). At different
180 time intervals, 5 mL of the suspension was collected and readily filtered through a
181 0.22 μm membrane to determine Mn, Ni, and Mg release. After 1 week of this HNO₃
182 treatment, residual samples were dried at 60 °C for 3 days and analyzed with X-ray
183 diffraction (XRD) at a scan speed of 10 ° 2θ .min⁻¹.

184 Mineralogy of all samples was determined from powder XRD analysis using a
185 Bruker D8 Advance diffractometer equipped with Cu Kα source (λ = 0.15418 nm)
186 and operated at 40 kV and 40 mA. XRD patterns were collected at 0.02 °2θ intervals
187 using a continuous scan mode. XRD data was collected on fresh samples (dried at
188 60 °C for three days) at a scan speed of 10 ° 2θ .min⁻¹. To assess the stability of their
189 hydration, XRD data was collected on fresh samples after heating to 140 °C. Finally,
190 XRD patterns were collected at 1 ° 2θ .min⁻¹ for aged samples that were kept dry in
191 the dark for three months. Synchrotron XRD patterns were also collected on selected
192 reflux products on beamline BL14B1 at the Shanghai Synchrotron Radiation Facility
193 (SSRF) and on beamline 4B9A at the Beijing Synchrotron Radiation Facility (BSRF).
194 At BSRF, XRD data was collected at the Mn K-edge (6.5 keV), Ni K-edge (8.3 keV),
195 and 12 keV with a typical beam size of 2 × 1 mm², whereas the 18 keV data was
196 collected at SSRF with a typical beam size of ~0.2 × 0.3 mm². In both cases, X-rays
197 were monochromatized with a double-crystal Si (111) monochromator. Finally,
198 high-energy X-ray scattering data was collected in transmission mode on beamline
199 11-ID-B at the Advanced Photon Source (Argonne National Laboratory, Argonne, IL),
200 using a ~90 keV X-ray energy. Pair distribution functions (PDF) and differential
201 PDFs were calculated as described elsewhere (Li et al., 2011; Wang et al., 2013).

202 Infrared spectra were collected for both layered precursors and reflux products
203 using a Bruker VERTEX 70. For each sample, 64 spectra were collected and summed
204 over the 4000–400 cm^{-1} range with a 4 cm^{-1} resolution (Zhao et al., 2015).
205 Micromorphology of the reflux products and lattice periodicities were observed a Jeol
206 JEM2100F transmission electron microscope (TEM) operated at 200 kV. TGA was
207 performed on a NETZSCH TG 209 instrument with a heating rate of 10 $^{\circ}\text{C min}^{-1}$ and
208 a N_2 flow of 20 mL min^{-1} . Finally, X-ray photoelectron O1s spectra were collected
209 with a VG Multilab2000. X-ray photoelectron spectroscopy (XPS) measurements
210 used an Al $\text{K}\alpha$ X-ray source (1486.6 eV) at a chamber base pressure of 3×10^{-9} Torr
211 (Yin et al., 2011a). The O 1s spectra were collected with a 25 eV pass energy and
212 0.1 eV energy steps, and analyzed with the Avantage software. All samples were
213 charge-corrected to C 1s with a binding energy of 284.80 eV collected from the
214 surface adventitious carbon (Wang et al., 2010). A Shirley-type background was
215 subtracted before deconvolution and fitting. A Lorentzian:Gaussian ratio of 30:70 was
216 used for all the fittings.

217 Finally, X-ray absorption spectra were collected at the Mn and Ni K-edges on the
218 1W1B beamline of BSRF to determine the relative proportions of Mn(II), Mn(III),
219 and Mn(IV) species and the local environments of Mn and Ni in both layered
220 precursors and reflux products. Data was recorded at room temperature in
221 transmission (Mn) and fluorescence (Ni) modes, and the energy was calibrated using
222 metallic Mn/Ni foils as references. Extended X-ray absorption fine structure (EXAFS)
223 spectra were processed using Athena and Artemis (Ravel and Newville, 2005). X-ray
224 absorption near-edge structure (XANES) spectra of both layered precursors and reflux
225 products were used to determine Mn average oxidation state (AOS) with a specific
226 linear combination fitting method (the so-called Combo method). Mn(II), Mn(III),
227 and Mn (IV) reference compounds were those of the original study (Table 1 in
228 Manceau et al., 2012).

229

230

3. RESULTS

3.1. Elemental composition

With increasing Ni content, the Mn content decreases from ~55.4 to ~44.8 wt.% for layered precursors and from ~54.4 to ~49.2 wt. % for reflux products (Table 1). The Ni/(Mn+Ni) molar ratios are essentially similar in layered precursors and their respective reflux products, with only a very limited fraction of Ni being lost either during the Mg-for-(Na,Ni) exchange or during the subsequent transformation process. In addition, the Mg wt.% in the reflux products significantly decreases from ~3.95 wt.% in the Ni-free Tod sample to ~2.11 wt.% in NiT20, thus suggesting a competition between Mg and Ni for interlayer and/or tunnel sites of layered precursors and/or of reflux products. Specific surface area (SSA) of NiT samples, as measured with the BET method, is systematically higher than that of Ni-free Tod, but no systematic evolution of SSA is observed with the increase of Ni content.

3.2. Powder X-ray diffraction

X-ray diffraction (XRD) patterns collected on fresh Bir (not shown) are essentially similar to those recorded after a few months of aging and display reflections at 7.2, 3.6, ~2.45, and ~1.42 Å, typical for birnessite (Drits et al., 1997; Lanson et al., 2002b). Similar reflections are observed for fresh NiB5 and NiB10 samples (Fig. S1), in addition to a broad maximum peaking at ~4.6 Å. The intensity of this maximum increases with increasing Ni concentration in the initial solution and is thus likely related to the presence of Ni (hydr)oxide (ICDD #13-0229), whose formation was reported under similar experimental conditions (oxidation of a Ni-rich alkaline solution – Feitknecht et al., 1956). Consistently, the intensity of this maximum is increased further for NiB15 and NiB20. These two samples exhibit also reflections at ~2.45, and ~1.42 Å, typical for layered manganates, the basal reflections

260 of which indicate a 9.9-10.0 Å layer-to-layer distance (Fig. S1). Upon moderate
261 heating (140 °C), these reflections shift to indicate a 7.2 Å layer-to-layer distance
262 typical for birnessite, as the result of interlayer cation partial dehydration (Golden et
263 al., 1986; Manceau et al., 1987; Drits et al., 1997). The initial presence of two planes
264 of interlayer H₂O molecules in NiB15 and NiB20 (buserite) is most likely indicative
265 of the presence of interlayer hydrated Ni(II) cations, whose hydration is reduced upon
266 heating. Sample heating also results in a decrease of the intensity of the ~4.6 Å
267 maximum.

268 After aging for about three months, all layered precursors but NiB20 display over
269 the low-angle region (5-30 °2θ) strong basal reflections at ~7.2 and ~3.6 Å typical for
270 birnessite and indicative of the spontaneous dehydration of NiB15 interlayers (Fig. 1).
271 Two planes of H₂O molecules are still present in most NiB20 interlayers (buserite),
272 however. Splitting of reflections at ~2.45 and ~1.42 Å, and more generally positions
273 of the reflections over the high-angle region (30-85 °2θ – Fig. 1), unambiguously
274 indicate that initial Bir is a triclinic birnessite (ICDD #43-1456), consistent with the
275 synthesis protocol (Lanson et al., 2002b). With increasing Ni content, high-angle
276 reflections broaden significantly thus indicating a decrease in the coherent scattering
277 domain size. In addition, the resolution of these reflections decreases also with
278 increasing Ni content, suggesting a minor increase of layer symmetry from orthogonal
279 ($a > b\sqrt{3}$, $\gamma = 90^\circ$) to hexagonal ($a = b\sqrt{3}$, $\gamma = 90^\circ$ – Yin et al., 2015). Positions of
280 birnessite *hkl* reflections remain essentially unchanged, however, indicative of the
281 persistence of the orthogonal layer symmetry in Ni-rich layered precursors. The broad
282 maximum at ~4.6 Å is present also in aged samples.

283 Reflux products systematically show reflections at ~9.6 Å, ~4.8 Å, ~3.2 Å,
284 ~2.46 Å, ~2.39 Å, ~2.22 Å, ~1.95 Å, ~1.73 Å, ~1.52 Å, and ~1.42-1.41 Å, that are
285 typical of todorokite (ICDD #38-0475 – Atkins et al., 2014, 2016). For the Ni-free
286 Tod, relative intensity of the three low-angle reflections (at ~9.6, ~4.8, and ~3.2 Å)
287 decreases in the order $I_{9.6} > I_{4.8} \gg I_{3.2}$, consistent with relative intensities of
288 todorokite 001/100, 002/200, and 003/300 reflections (Post et al., 2003), respectively.
289 With increasing Ni content, the positions of both ~9.6 and ~4.8 Å reflections shift

290 towards higher angles for NiT15 and NiT20, compared to Ni-free Tod (Fig. S2) and
291 the ~ 4.8 Å reflection becomes predominant, consistent with previous reports of
292 todorokite prepared in the presence of various divalent metals (Shen et al., 1993, 1994;
293 Ching et al., 1999; Nicolas-Tolentino et al., 1999; Fuertes et al., 2012) and
294 asymmetric. Although not described as such in these references, this intensity ratio
295 modification is consistent with the presence of asbolane, a phyllosulfate with an
296 incomplete – island-like – octahedral layer of metal (hydr)oxides in the interlayer
297 (Chukhrov et al., 1987; Golden et al., 1987; Fan and Gerson, 2015). The presence of
298 these incomplete brucite-like octahedral layers between MnO₂ layers precludes the
299 collapse of the layer-to-layer distance to ~ 7.2 Å upon heating (Fig. S3)

300

301 3.3. Anomalous XRD patterns

302

303 To investigate further the possible origin of the observed contrasting $I_{4,8}/I_{9,6}$
304 intensity ratios, XRD patterns of Tod, NiT15, and NiT20 were recorded at different
305 energies, including Mn and Ni K-edges to modify the contribution of these elements
306 to the structure factor (F_{hkl}). These XRD patterns logically exhibit reflections at
307 similar d-values (Fig. 2a-d). Except for the pattern recorded at the Mn K-edge all Tod
308 patterns also display similar low $I_{4,8}/I_{9,6}$ intensity ratios (Fig. S4), consistent with
309 previous reports (Shen et al., 2011). Contrastingly, the $I_{4,8}/I_{9,6}$ intensity ratio is
310 significantly higher for NiT15 and NiT20 compared to Tod, and varies significantly
311 for these two samples as a function of the energy used for data collection. Specifically,
312 NiT15 and NiT20 display highest $I_{4,8}/I_{9,6}$ intensity ratios at the Mn K-edge and lowest
313 ratios at the Ni K-edge, whereas similar ratios are obtained for XRD patterns recorded
314 at energies different from the two absorption edges (Figs. 2a-d; S4). Both features
315 indicate contrasting structures of Tod and Ni-rich NiT products depending on the
316 initial Ni content.

317 As reported in the early descriptions of asbolane, this compound exhibits high
318 values of the $I_{4,8}/I_{9,6}$ intensity ratio (Chukhrov, 1982; Llorca, 1988; Fan and Gerson,
319 2015), consistent with XRD patterns calculated for such a structure hosting an

320 incomplete Ni(OH)₂ layer sandwiched in between two MnO₂ layers (Fig. 2e). In
321 addition, for a given composition, this ratio increases when the contribution of Mn
322 atoms to the structure factor is reduced (XRD data recorded at the Mn K-edge – Fig.
323 2a) and decreases when the contribution of Ni atoms to the structure factor is reduced
324 (XRD data recorded at the Ni K-edge – Fig. 2b), consistent with the data. In addition,
325 this ratio increases with the completeness of interlayer plane (Fig. 2e). Together with
326 the collapse of layer-to-layer distance upon acid-dissolution of the incomplete
327 Ni(OH)₂ layer (see below), these variations of the I_{4.8}/I_{9.6} intensity ratio can be
328 ascribed to the presence of asbolane, rather than todorokite, in the reflux products.

329

330 3.4. FTIR

331

332 FTIR spectra of todorokite and of other 3×n tectomanganates display a band at
333 ~760 cm⁻¹, typical for the corner-sharing linkage in their structures (Fig. 3 – Golden et
334 al., 1986; Feng et al., 2004; Julien et al., 2004; Atkins et al., 2014; Zhao et al., 2015).
335 This band is clearly visible in Tod FTIR spectrum but steadily decreases in intensity
336 with increasing Ni content, most likely as the result of the decreasing proportion of
337 3×n tectomanganates in Ni-rich reflux products. Consistent with their layered
338 structure, this band is absent in FTIR spectra of layered precursors. Rather, two lines
339 at ~820 and ~950 cm⁻¹ are visible in the FTIR spectra of Ni-containing layered
340 precursors. These two lines are visible also in the spectra of related reflux products,
341 although their intensity is reduced after the reflux treatment. The peak at ~820 cm⁻¹
342 visible in NiB and NiT was identified as a combination lattice mode band in Ni
343 (hydr)oxides (Hall et al., 2015), which is consistent with the XRD analysis.

344

345 3.5. HRTEM

346

347 Consistent with previous studies (Turner and Buseck, 1981; Golden et al., 1986;
348 Shen et al., 1993; Feng et al., 2004; Wu et al., 2019), crystals with fibrous and
349 plate-like morphologies are systematically present in the reflux products (Fig. 4), the

350 former dominating in Tod and NiT1 (Figs. 4a-c), whereas platy crystals dominate
351 samples having higher Ni-contents (NiT5 and NiT15; Figs. 4f, i). Fiber-shaped
352 crystals (Figs. 4 e, g, h) often display lattice fringes with a typical ~1 nm periodicity,
353 corresponding to the 3×3 todorokite tunnel structure (Golden et al., 1986; Feng et al.,
354 2004). As it is common in todorokite, fibers are often aligned at $\pm 120^\circ$ with respect to
355 each other, thus forming trilling patterns (Siegel and Turner, 1983; Golden et al., 1986;
356 Feng et al., 2004; Bodei et al., 2007; Xu et al., 2010; Atkins et al., 2014). Visible
357 lattice fringes in the plates are commonly more diverse than in the fibers (Figs. 4 b, d
358 and j), typical for α -disordered todorokite (Xu et al., 2010; Wu et al., 2019). Lattice
359 fringes are also visible in short rods and small plates, indicating the initial
360 development of tunnel structure therein (Figs. 4 g, h – Golden et al., 1986). Finally,
361 smooth surfaces without visible fringes, that are most likely typical for
362 phyllomanganate crystals (Golden et al., 1986, 1987; Wu et al., 2019), are also visible
363 (Figs. 4 g – zone 4, 4i, j – zone 1, 4k – zone 5). Interestingly, some platy particles
364 exhibit lattice fringes over specific zones with smooth surfaces (Figs. 4g, j). This dual
365 character is possibly related to the initial development of tunnel structures in specific
366 zones of the particles whereas other zones maintain their initial planar structure
367 (Golden et al., 1987; Wu et al., 2019).

368

369 3.6. Nitric acid treatment

370

371 Upon equilibration in nitric acid, Mn release from layered precursors reaches
372 equilibrium within 12 hrs, the proportion of Mn released from NiB is higher than that
373 released from Bir, (Fig. 5a), possibly as an effect of reduced crystal size. For reflux
374 products, the release of Mn is slower, reaching equilibrium after ~48 hrs, and is
375 essentially the same for all NiT samples (Fig. 5b), except for NiT5. Ni release is much
376 slower than that of Mn, reaching a plateau after ~168 hrs in both layered precursors
377 (Fig. 5c) and reflux products (Fig. 5d). The proportion of Ni released differs however
378 in the two series of samples as essentially all Ni is released from layered precursors
379 whereas ~20% of Ni remains in the reflux products, possibly indicative of Ni

380 structural incorporation. Finally, Mg is systematically totally released from reflux
381 products, possibly at a slower rate with increasing Ni content (Fig. 5f).

382 After acid treatment, the XRD pattern of Tod is essentially alike that of the initial
383 reflux product and typical for todorokite (Fig. 5e). On the other hand, XRD patterns
384 recorded on NiT15 and NiT20 after acid treatment exhibit, over the low-angle region,
385 peaks at ~ 7.2 and ~ 3.6 Å, typical for the phyllomanganate birnessite, rather than
386 peaks at ~ 9.6 , ~ 4.8 , and ~ 3.2 Å, as expected for todorokite (Fig. 5e). These two XRD
387 patterns are actually similar to the one recorded on Bir after acid treatment and match
388 XRD pattern of hexagonal birnessite (ICDD #23-1239), which was obtained from the
389 low-pH equilibration of an initial triclinic birnessite (Lanson et al., 2000). The
390 evolution of XRD patterns recorded from reflux products upon acid treatment is
391 consistent with that observed for an asbolane-like phyllomanganate (Wu et al., 2019).
392 The structure of these ~ 9.6 Å phyllomanganates consists of an octahedral MnO_2 layer
393 similar to that of birnessite, with an incomplete octahedral $\text{Me}(\text{OH})_2$, MeOOH , or
394 MeO_2 sheet, possibly incommensurate with the MnO_2 layer, in the interlayer
395 (Chukhrov, 1982; Manceau et al., 1987; Fan and Gerson, 2015). This incomplete
396 interlayer octahedral sheet is solubilized by the acid treatment leading to the observed
397 7.2 Å layer-to-layer distance (Wu et al., 2019). Such a peak at ~ 7.2 Å is visible in the
398 XRD pattern of acid-treated NiT5 and NiT10, and its intensity increases with
399 increasing Ni content, becoming the sole visible diffraction signature in acid-treated
400 NiT15 and NiT20 (Fig. 5e).

401

402 3.7. Thermogravimetric analysis

403

404 Thermogravimetric analyses of layered precursors systematically show a
405 significant weight loss at 140 - 150 °C corresponding to the dehydration of interlayer
406 Na^+ and Ni^{2+} cations, this weight loss decreasing with increasing Ni content (Figs. 6a,
407 c; Table 2). A minor weight loss (2.4 - 2.9% in Bir, NiB5, NiB10, and NiB15) is also
408 observed for these samples below 100 °C, which is most likely related to the
409 departure of adsorbed water (Gaillot et al., 2003). This low-temperature weight loss is

410 significantly increased for NiB20 (9.25%), however, most likely as the result of a
411 low-temperature buserite-to-birnessite transition associated with the loss of one plane
412 of interlayer H₂O molecules as observed during moderate heating of fresh NiB
413 samples (Fig. S1). A significant weight loss (4.10 and 6.72% for NiB5 and NiB20,
414 respectively) is observed also for NiB samples over the 170-400 °C range. This
415 weight loss is essentially absent in the TGA curve of Bir (1.78%) and increases with
416 Ni content. It is likely related to the presence of the Ni (hydr)oxide responsible for the
417 broad XRD maximum peaking at ~4.6 Å (Fig. 1). Finally, a weight loss is observed at
418 ~550 °C for all layered precursors, with no significant influence of the Ni content,
419 probably indicating the reduction of MnO₂ to Mn₂O₃ (Bish and Post, 1989).

420 TGA curves recorded for reflux products significantly differ from those of their
421 layered precursors, with weight losses at ~150, ~285, ~440, and ~545 °C for Tod
422 (Figs. 6b, d). The weight loss observed from ~110-240 °C is most likely related to the
423 loss of the H₂O molecules hydrating cations present in todorokite tunnels (Bish and
424 Post, 1989). With increasing Ni content, this weight loss decreases (from 8.05 to 6.12%
425 in Tod and NiT20, respectively) and shifts towards lower temperatures, most likely
426 indicative of the mineralogical evolution evidenced by XRD data recorded on
427 acid-treated reflux products (Fig. 5e). For NiT10, this low-temperature weight loss
428 splits in a doublet owing to the coexistence of todorokite and asbolane (Fig. 5e). The
429 weight loss occurring at ~285 °C is also ascribed to the departure of tunnel water
430 (Bish and Post, 1989). TGA curves obtained for Tod and NiT20 also differ
431 significantly over this range, with a shift of the weight loss towards higher
432 temperatures in NiT20 compared to Tod. Evolution with increasing Ni content, is not
433 as systematic as that observed for the low-temperature weight loss, however (Fig. 6d).
434 The third weight loss occurring at ~440 °C appears as a distinct signature for the
435 presence of todorokite, as its intensity decreases with increasing Ni content to vanish
436 for NiT15 and NiT20 which essentially contain asbolane (Fig. 5e). A last weight loss
437 occurs at 520-550 °C, a temperature similar to that reported for layered precursors at
438 ~550 °C (Figs. 6b, d).

439

440 3.8. O1s X-ray photoelectron spectroscopy

441

442 Consistent with the systematic prevalence of $[\text{MnO}_6]$ building octahedral in both
443 phyllomanganates and tectomanganates, all O1s XPS spectra are dominated by a peak
444 at ~ 529.6 eV (Fig. 7), typical for oxygen (O^{2-}) in metal oxides. This main peak is
445 asymmetric and displays a tail on its high-energy side for both layered precursors and
446 reflux products. This tail at ~ 531 - 535 eV can be decomposed into the contributions of
447 oxygen atoms from hydroxyl groups (OH^- ; 530.9 - 531.6 eV) and from water
448 molecules (532.2 - 533.4 eV). For layered precursors, the intensity of this tail, and
449 more especially that of the OH^- contribution, increases with increasing Ni content (Fig.
450 7; Table S1), whereas the H_2O contribution is about constant for all NiB samples but
451 NiB20 that shows a slightly higher proportion of O atoms from H_2O molecules,
452 consistent with TGA data. In reflux products the contribution of O atoms in hydroxyl
453 groups is significantly higher in NiT samples compared to Tod, consistent with the
454 presence of asbolane-like phyllomanganate in Ni-rich reaction products. On the other
455 hand, the H_2O contribution shows no systematic evolution with Ni content (Fig. 7;
456 Table S1). Finally, relative intensities of peaks corresponding to OH^- and H_2O
457 contributions are significantly increased in NiT samples compared to their
458 corresponding layered precursors, at least under the deep vacuum conditions
459 prevailing during the XPS measurements.

460

461 3.9. X-ray absorption spectroscopy

462

463 3.9.1. Mn K-edge XANES

464 Relative proportions of Mn(II), Mn(III), and Mn(IV) species and Mn average
465 oxidation state (AOS) have been determined using the Combo method (Table 3 –
466 Manceau et al., 2012). Results consistently indicate high ($\sim 1/3$) relative proportions of
467 Mn(III) in both layered precursors and reflux products, which is considered a key
468 condition for the phyllomanganate-to-tectomanganate conversion (Cui et al., 2008;
469 Atkins et al., 2014, 2016; Grangeon et al., 2014, 2015; Zhao et al., 2015; Li et al.,

470 2016). The measured proportion of Mn(III) is slightly lower in Ni-free samples
471 compared to the Ni-bearing ones (Table 3) and no significant difference is observed
472 between layered precursors and their reflux products. In all cases, the Mn(II) content
473 is null within the experimental error.

474

475 3.9.2. Mn K-edge EXAFS

476 EXAFS spectra of both layered precursors and of reflux products show
477 significant evolutions with increasing Ni content, thus indicating that the presence of
478 Ni affects the local structure of manganates in the two series of samples (Fig. 8). The
479 EXAFS spectrum collected for Ni-free layered precursor (Bir) is typical for triclinic
480 birnessite over both the staircase and the indicator regions (3.5-6.0 Å⁻¹ and
481 7.5-10.0 Å⁻¹, respectively – Marcus et al., 2004). In particular, the splitting of the
482 features at ~7.8 Å⁻¹ and ~9.0 Å⁻¹ (arrows in Fig. 8a) are indicative of a high Mn(III)
483 content, of the systematic elongation of Mn(III) octahedra along the *a* axis, and of
484 their ordered distribution in rows parallel to the *b* axis (Marcus et al., 2004; Gaillot et
485 al., 2007), typical features for triclinic birnessite (Webb, 2005; Atkins et al., 2014; Yin
486 et al., 2014). With increasing Ni content, the ~7.8 Å⁻¹ feature becomes less
487 pronounced even though its position remains unchanged, consistent with the similar
488 Mn(III) contents of all layered precursors (Table 3) and with the similar overall
489 frequency of the EXAFS spectra of these samples (Gaillot et al., 2007). The steady
490 lowering of the ~7.8 Å⁻¹ feature resolution is thus most likely related either to disorder
491 in the distribution of elongated Mn(III) octahedral or to some randomness in the
492 direction of the elongation, consistent with the evolution of XRD patterns with
493 increasing Ni content. The split ~9.0 Å⁻¹ feature observed for Bir and NiB1 also turns
494 into a broad and more symmetrical feature with increasing Ni content and the induced
495 vanishing of the sharp high-frequency contribution.

496 In k-space Mn K-edge EXAFS spectra of Tod and NiT1 exhibit sharp features at
497 ~8.0 and ~9.2 Å⁻¹ that are typical for todorokite (Webb, 2005; Bodeř et al., 2007; Feng
498 et al., 2010; Atkins et al., 2014). These two features essentially decrease in intensity at
499 higher Ni content. In addition, the ~9.2 Å⁻¹ feature shifts to lower wave numbers in

500 NiT samples compared to Tod and NiB1 (Fig. 8b). EXAFS spectra of Ni-rich NiT
501 samples and their Fourier transforms (FTs) are actually alike those of their
502 corresponding layered precursors (Figs. 9a-b), consistent with the similar structure of
503 the MnO₂ layer in both birnessite and asbolane. On the contrary, spectra obtained for
504 Ni-free Bir and Tod differ significantly, as expected for layered and tunnel manganese
505 oxides (Fig. 9c). In particular, the FTs of these spectra show a clear shortening of the
506 average Mn-Me_E distance in Tod compared to Bir, as shown by the shift of the
507 imaginary part of the FT (Fig. 9d, arrow). In addition, Tod FT shows a clear
508 maximum at $R + \Delta R \sim 3.0 \text{ \AA}$, typical of Mn-Me_C pairs, which is not observed for its
509 Bir precursor. For both Ni-free and Ni-rich samples, Mn-O distances are similar in
510 both layered precursors and corresponding reflux products, consistent with their
511 similar Mn AOS.

512

513 3.9.3. Ni K-edge EXAFS

514 EXAFS spectra collected at the Ni K-edge are similar for both NiB samples, on
515 the one hand, and NiT, on the other hand (Fig. 10), thus implying similar Ni
516 speciation in each of the two sample groups. Although it was not possible to obtain a
517 decent fit to this data using a linear combination fitting and available Ni reference
518 spectra, similarity of the hydrated Ni(II) spectrum with collected spectra suggests that
519 this species possibly prevails in all samples. In addition, the evolution of Ni speciation
520 during the reflux process was assessed by fitting EXAFS spectra of reflux products as
521 a linear combination of their respective NiB precursors and of Ni reference spectra
522 (Fig. S4). For all NiT samples, a good fit was obtained with ~15% of a Ni(OH)₂
523 contribution in addition to the layered precursor (Table S2), consistent with the
524 polymerization of a partial Ni(OH)₂ layer in birnessite interlayers to form an
525 asbolane-like structure.

526

527 3.10. Pair distribution functions (G(r))

528

529 Atomic PDFs computed from Tod, NiT10, and NiT20 high-energy X-ray

530 scattering patterns show similar peak positions (Fig. 11), indicative of similar local
531 structures (Zhu et al., 2012) as expected from the major contribution of layers/ribbons
532 of edge-sharing MnO_6 octahedra in both layered precursors and reflux products.
533 Consistently, the maxima at $\sim 1.90 \text{ \AA}$, $\sim 2.90 \text{ \AA}$, and $\sim 3.50 \text{ \AA}$ essentially correspond to
534 the first neighbor Mn-O, to edge-sharing Mn-Me, and to a combination of
535 corner-sharing Mn-Me and of second neighbor Mn-O atomic pairs, respectively (Zhu
536 et al., 2012). The increased intensity of the $\sim 3.50 \text{ \AA}$ maximum and the decreased
537 intensity of the one at $\sim 5.00 \text{ \AA}$ in the PDF of Tod compared to NiT10 and NiT20 are
538 typical of the prevalence of tunnel structures in the former sample and of layered
539 structures in the latter (Grangeon et al., 2015). The $\sim 5.00 \text{ \AA}$ maximum is mainly
540 related indeed to second neighbor Mn-Mn pairs (Fig. S4 – Zhu et al., 2012), that are
541 favored by the lateral extension of MnO_2 layers. Finally, the peak at $\sim 4.50 \text{ \AA}$ is most
542 likely related to Mn2-Mn2 and Mn4-Mn4 pairs across “holes” in tunnel walls, floors,
543 and ceilings (Fig. S6), consistent with the increased intensity of this $\sim 4.50 \text{ \AA}$ peak
544 with decreasing tunnel size (Zhu et al., 2012).

545 Differential PDF (d-PDF) can be calculated to assess more precisely the specific
546 modifications affecting the reflux products, and more especially the broadening of the
547 ~ 1.90 and 2.90 \AA peaks towards high d-values with increasing Ni content (Fig. 11).
548 The d-PDF curves obtained for NiT10 and NiT20, both show a first peak at $\sim 2.05 \text{ \AA}$
549 typical for Ni-O pairs (Manceau et al., 2007a,b; Peacock and Sherman, 2007a,b; Yin
550 et al., 2012; Kwon et al., 2013; Simanova et al., 2015; Atkins et al., 2016). A second
551 peak, similar in both d-PDF curves, is visible at $\sim 3.05 \text{ \AA}$. This second peak is
552 intermediate between those calculated Ni-Ni pairs in NiO and Ni(OH)_2 , consistent
553 with the presence of both compounds in the reflux products identified from XRD data
554 (Figs. 1, 2).

555

556

4. DISCUSSION

557

558 **4.1. Structural transformation of layered precursors**

559

560 Addition of Ni during the synthesis of layered precursors does not impact
561 significantly their crystal structure. In particular, the Mn(III) content of layered
562 precursors remains about constant at $\sim 1/3$ (Table 3) whatever the initial Ni content.
563 Consistently, XRD results (Fig. 1) show that layer symmetry remains orthogonal ($a >$
564 $b\sqrt{3}$) for all precursors, indicative of the systematic elongation of distorted Mn(III)
565 octahedra along the a axis and of their ordered distribution. FTs of the EXAFS spectra
566 consistently show similar Mn-Me_E distances in all layered precursors (not shown).
567 Both XRD patterns and EXAFS spectra of layered precursors are significantly
568 modified when increasing the Ni content, however. These changes reveal an increased
569 disorder in the orientation of Mn(III) octahedra and/or in their distribution.

570 The increasing intensity of the ~ 4.6 Å diffraction maximum with increasing Ni
571 content indicates that part of Ni initially introduced in solution actually precipitates as
572 Ni (hydr)oxide. The presence of Ni in the interlayers of NiB15 and NiB20 is attested
573 by the presence of two planes of interlayer water molecules, consistent with its more
574 negative hydration enthalpy compared to Na⁺ (Smith, 1977; Johnson and Post, 2006),
575 in these fresh samples. All Ni species, including the two mentioned above, are readily
576 mobilized by the acid treatment (Fig. 5c), and it is thus reasonable to hypothesize that
577 no Ni(II) cations are incorporated in the octahedral layer. Similarly, the orthogonal
578 layer symmetry is typical of octahedral layers containing few vacant layer sites (Drits
579 et al., 1998; Lanson et al., 2000), if any, and the presence of Ni(II) cations sorbed
580 above or below such vacant sites is thus unlikely.

581 Although weakly bound to the layered precursors, the presence of Ni(II)
582 significantly impacts their transformation during the reflux process. Bir, a typical
583 triclinic birnessite, converts readily and completely to an α -disorder todorokite (Wu et
584 al., 2019). With increasing Ni content, disorder increases together with the proportion
585 of non-ideal $3 \times n$ tunnel sizes forming trilling patterns. In addition, platy crystals are
586 visible in all reflux products, their relative abundance increasing with increasing Ni
587 content with only minimal fragments of tunnel oxides being detected in NiT15 and
588 NiT20 (Fig. 4). Platy crystals are most likely asbolane, as shown by the prevalence of

589 this phyllomanganate hosting an incomplete octahedral layer of metal (hydr)oxides in
590 their interlayers in Ni-rich reflux products. These incomplete brucite-like octahedral
591 layers are dissolved by the acid treatment, leading to birnessite-like structures (Fig.
592 5e). As reported in the early work of Chukhrov and coworkers on natural asbolane
593 (Chukhrov, 1982; Chukhrov et al., 1987), XRD diffraction patterns of asbolane are
594 characterized by high $I_{4.8}/I_{9.6}$ intensity ratios. Such high $I_{4.8}/I_{9.6}$ intensity ratios are
595 commonly reported for “todorokite”, especially when synthesized in the presence of
596 metallic elements such as Co, Ni, Cu, Zn, Er, La, etc (Shen et al., 1994; Tian et al.,
597 1997; Ching et al., 1999; Luo et al., 1999). In the present study, the combined use of
598 XRD simulation, anomalous XRD, HRTEM, thermogravimetric analysis, and nitric
599 acid treatment allowed uncovering the actual nature of this seldom described
600 phyllomanganate, but its formation may be far more common than previously
601 reported in these experimental studies.

602 As shown in Fig. 2e, this $I_{4.8}/I_{9.6}$ intensity ratio strongly depends on the
603 completeness of the interlayer brucite-like octahedral layer, and the ratio determined
604 for NiT15 and NiT20 corresponds to a ~50% completeness of the $\text{Ni}(\text{OH})_2$ octahedral
605 layer. This interlayer occupancy is much higher than possibly achieved with the sole
606 presence of Ni(II) in these octahedral layers as Ni / (Ni+Mn) ratios are 8-12% in these
607 samples, with part of the Ni present as Ni (hydr)oxide. It is thus likely that Mg cations
608 contribute to the electron density at the interlayer mid-plane, in addition to Ni. As Mg
609 scattering factor is lower than that of Ni, the actual completeness of the interlayer
610 brucite-like layer is likely higher than 50%.

611

612 **4.2. Differentiation of asbolane and todorokite.**

613

614 Although the $I_{4.8}/I_{9.6}$ intensity ratio strongly depends on the completeness of the
615 interlayer brucite-like octahedral layer, a 4.8 Å peak stronger than its 9.6 Å
616 counterpart is a possible indication of the presence of the phyllomanganate asbolane,
617 rather than the tectomanganate todorokite, in reaction products, or in natural samples.
618 The two compounds indeed share these two interplanar distances. With its two planes

619 of interlayer H₂O molecules, busserite also exhibits similar periodicity but a gentle
620 heating (to ~100°C) should lead to the partial dehydration of interlayer cations and to
621 the ~7.2 Å periodicity typical of birnessite (Fig. S1 – Johnson and Post, 2006).
622 Furthermore, busserite is unlikely to have a high enough content of interlayer cations
623 to induce a I_{4.8}/I_{9.6} ratio higher than 1.0.

624 Although values of this ratio higher than 1.0 are typically observed for asbolane,
625 the partial exchange of Mg present in todorokite tunnels by cations having a higher
626 electronic content (such as Ni and other divalent metal cations) can also lead to such
627 high I_{4.8}/I_{9.6} ratios (Fig. 11), thus not allowing an unambiguous differentiation
628 between asbolane and todorokite. In this search for an unquestionable differentiation
629 between asbolane and todorokite, the nitric acid treatment proposed by Wu et al.
630 (2019) thus appears as a simple and reliable method. In the case of asbolane,
631 dissolution of the interlayer brucite-like layer induced by the treatment leads indeed to
632 a collapse of the layer-to-layer distance to the ~7.2 Å periodicity. On the contrary,
633 periodicities are maintained for todorokite, the tectomanganate framework being
634 unaltered, and positions of XRD maxima are thus unchanged.

635

636 **4.3. The role of Mn(III) and interlayer species during the transformation**

637

638 It is now accepted that the presence of a high Mn(III) content (>25-30%) in
639 layered precursors is required for their conversion to tectomanganates. This pivotal
640 role is most likely related to the steric strains induced by the presence of Jahn-Teller
641 distorted Mn(III) octahedra in the octahedral layers. Migration of these Mn(III)
642 cations from layer to interlayer or layer kinking at these structurally weak points
643 contribute to building tunnel walls (Grangeon et al., 2008, 2014; Atkins et al., 2014,
644 2016; Yang et al., 2018). In the present case, the ordered distribution of Mn(III)
645 cations in rows parallel to the *b* axis and separated from each other along the *a* axis by
646 two rows of Mn(IV) creates a structurally weak point favorable to the formation of
647 tunnels walls (Atkins et al., 2014; Grangeon et al., 2014). Consistently, the initial
648 Ni-free precursor Bir, a triclinic birnessite, was fully converted to todorokite. Similar

649 transformation of triclinic birnessite to tunnel structures was previously reported in
650 the literature although 3×3 tunnels were not systematically obtained (Yang et al.,
651 2018). Furthermore, the actual distribution and orientation of Mn(III) octahedra
652 present in the MnO₂ layer do not appear to be key factors for the
653 phylломanganate-to-tectomanganate conversion as tectomanganates were obtained
654 from hexagonal birnessite precursors in which Mn(III) octahedra are distributed
655 and/or oriented at random (Grangeon et al., 2008, 2014; Atkins et al., 2014, 2016;
656 Zhao et al., 2015). The absence of transformation of NiB precursors to tunnel
657 structures thus does not appear to be related to their Mn(III) content, which is similar
658 to or higher than that of the Ni-free Bir.

659 As layers of all NiB precursors are essentially devoid of Ni, both in the octahedral
660 layer and sorbed above/below vacant layer sites, the absence of transformation of
661 these precursors to tunnel structures is thus likely due to kinetic effects favoring the
662 formation of asbolane. Specifically, polymerization of Ni as Ni(OH)₂ fragments in the
663 interlayers of initial birnessite/buserite (Fig. S5, Table S2) is favored over the
664 conversion to tectomanganates. In turn, the presence of interlayer Ni(OH)₂ fragments
665 likely impedes the migration of Mn(III) from the layer to the interlayer thus
666 preventing the conversion to tectomanganates. Such competing effects are supported
667 also by the increase of (Mg + Ni)/Mn ratios with increasing Ni content (Table 1) and
668 are likely to occur with a variety of other hydrolysable metal cations. Consistently,
669 “todorokite” containing divalent metal cations and displaying high I_{4.8}/I_{9.6} ratios
670 possibly indicate the presence of asbolane-like structure. Such competing effects
671 might contribute also to the prevalence of phylломanganates over tectomanganates in
672 natural environments (Wu et al., 2019).

673

674 **4.4. Negative influence of Ni and Co on the phyllo-to-tectomanganate** 675 **transformation: Contrasting mechanisms**

676

677 Both in the present work investigating the possible transformation of
678 Ni-containing layered precursors to tectomanganates and in the related study

679 investigating a similar process for Co-containing layered precursors, tectomanganate
680 formation was inhibited, totally (Ni) or partially (Co) for Me-rich precursors. The
681 origin of these similar negative impacts differs however for the two metals. In the
682 present case, layered precursors contain sufficient amounts of Mn(III) (~1/3) to
683 trigger the transformation, as Ni(II) is not structurally incorporated in the precursors.
684 As discussed above, polymerization of Ni(OH)₂ fragments in birnessite interlayers is
685 kinetically favored over migration of Mn(III) from the layer to the interlayer, or layer
686 kinking, however, leading to the formation of asbolane rather than tectomanganates.
687 In contrast and consistent with previous reports (Manceau et al., 1997; Yu et al., 2012;
688 Kwon et al., 2013; Simanova and Pena, 2015; Yin et al., 2015), Co(II) is readily
689 oxidized by birnessite during the formation of initial layered precursors with Co(III)
690 being structurally incorporated in these precursors owing to the similar ionic radii of
691 Co(III) and Mn(IV) (Wu et al., 2019). The symmetry of layered precursors is
692 increased from orthogonal to hexagonal. As a consequence, the content of Mn(III) in
693 Co-containing layered precursors is lowered and does not allow triggering the
694 transformation to tunnel structures (Grangeon et al., 2008, 2014; Atkins et al., 2014,
695 2016). In both cases, little Me is released to solution during the reflux process and Me
696 cations are structurally incorporated in the reflux products (~20% and ~80% for Ni
697 and Co, from the nitric acid experiments and EXAFS simulation, respectively) thus
698 enhancing their sequestration in both tecto- and phyllomanganates.

699

700 **4.5. The fate of Nickel during the transformation of layered precursors**

701

702 Previous studies have consistently shown that Ni can be incorporated in the
703 birnessite structure, either within the octahedral layer or sorbed at vacant layers sites
704 (Peacock and Sherman, 2007b; Grangeon et al., 2008, 2017; Peacock, 2009; Peña et
705 al., 2010; Yin et al., 2012; Kwon et al., 2013; Yin et al., 2014; Simanova et al., 2015;
706 Atkins et al., 2016; Lefkowitz and Elzinga, 2017), consistent with natural occurrences
707 (Bodeř et al., 2007; Manceau et al., 2007a,b; Peacock and Sherman, 2007a). In their
708 literature review, Grangeon et al. (2017) showed that the fraction of Ni structurally

709 incorporated in birnessite octahedral layers may be high (up to ~50%) only for low Ni
710 content (~1%), as reported for natural samples (Bodeř et al., 2007; Manceau et al.,
711 2007a,b; Peacock and Sherman, 2007a). Structural incorporation of Ni(II) in the
712 octahedral layer appears to be enhanced by circumneutral pH conditions and time
713 (Manceau et al., 2007b; Peacock and Sherman, 2007b; Peacock, 2009; Peña et al.,
714 2010). Competitive sorption at TCS/DCS sites has been proposed also as a
715 mechanism favoring structural incorporation in the octahedral layer (Lefkowitz and
716 Elzinga, 2017). Some studies report the prevalence of Ni sorbed at TCS/DCS sites
717 even for Ni/Mn ratios higher than 10%, however (Manceau et al., 2007a,b; Peña et al.,
718 2010; Yin et al., 2012; Simanova et al., 2015; Grangeon et al., 2017). In such cases,
719 sorption of Ni(II) as inner sphere complexes is favored by the presence of vacant
720 octahedral sites and is thus negatively correlated with the Mn(III) content.
721 Consistently, in our study structural incorporation of Ni in vacancy-free NiB
722 precursors appears very limited. In NiB layered precursors, Ni is rather present both
723 as Ni (hydr)oxide and as hydrated cations in birnessite/buserite interlayers, as shown
724 by the increased hydration of Ni-rich precursors (Figs. 1, S1). The influence of Ni on
725 phylломanganate hydration has been reported also for natural samples in which
726 buserite (or 10 Å vernadite) abundance increases with increasing Ni content (Bodeř et
727 al., 2007; Manceau et al., 2007a).

728 As discussed above, hydrated Ni(II) initially present in birnessite interlayers are
729 readily stabilized during the reflux products by forming Ni(OH)₂ fragments (Fig. S5,
730 Table S2), consistent with previous experiments with vacancy-free phylломanganate
731 precursors (Feng et al., 2001). Polymerization of Ni(OH)₂ brucite-like octahedral
732 layers in phylломanganate interlayers is consistent also with the natural predominance
733 of asbolane in Ni-rich environments (NiO ~10-20 wt.%, – Chukhrov, 1982; Chukhrov
734 et al., 1987; Roque-Rosell et al., 2010; Ploquin et al., 2018) . Although the Mn AOS
735 of his synthetic samples (~4.0) was favorable for Ni sorption at layer vacancy sites,
736 Manceau et al. (2007b) also reported the overwhelming presence of Ni as Ni(OH)₂ at
737 high Ni content (Ni/Mn ratio of ~0.10 and ~0.18 at pH 4 and 7, respectively), despite
738 experimental conditions supposed to prevent Ni(OH)₂ precipitation. The reflux

739 process appears to have little influence on the Ni (hydr)oxide formed together with
740 the layered precursors, as evidenced by the stability of the corresponding maximum at
741 $\sim 4.6 \text{ \AA}$ in the reflux products (Fig. 1b). Finally, part of Ni ($\sim 20 \%$) is stabilized during
742 the reflux process, as shown by the incomplete Ni release during acid treatment (Fig.
743 5d). Stabilized Ni is possibly structurally incorporated in the reflux products. On the
744 contrary, Atkins et al. (2016) reported no structural incorporation of Ni(II) during the
745 formation of todorokite from a Ni-bearing birnessite precursor ($\sim 1 \text{ wt\% Ni}$ in
746 hexagonal birnessite). They reported also a decrease in the Ni content of their reflux
747 products, whereas in our experimental conditions stability of Ni/(Mn+Ni) ratios
748 (Table 1) indicates that all Ni initially present in layered precursors is retained during
749 the reflux process.

750

751 5. CONCLUSION

752

753 The present study reports on the association of weakly bound Ni species
754 (hydrated Ni, Ni (hydr)oxides) with phylломanganates, that possibly prevail in natural
755 Ni-rich ($>10\% \text{ NiO}$) manganates. Whatever their Ni content, prepared
756 phylломanganates systematically exhibit an orthogonal layer symmetry, indicative of
757 a high Mn(III) content and of a minimal number of octahedral layer vacancies. Ni is
758 essentially present as charge-compensating hydrated Ni(II) and as Ni (hydr)oxide,
759 with no detectable Ni(II) sorbed or structurally incorporated in the phylломanganate
760 structure.

761 Despite their high content of Mn(III), a favorable condition for their conversion
762 to tectomanganates, asbolane rather than tectomanganates forms during the reflux
763 processing of these Ni-rich phylломanganates. Asbolane formation results from the
764 kinetically favored polymerization of fragments of Ni(OH)₂ octahedral layers in
765 birnessite interlayers. The structure of the initial manganate layers is essentially
766 unaffected by this transformation.

767 Formation of asbolane, rather than todorokite, may actually be more frequent than

768 reported in the literature owing to the similar periodicities in both compounds. High
769 values (> 1) of the $I_{4.8}/I_{9.6}$ intensity ratio may suggest the presence of this seldom
770 described phyllomanganate. Acid nitric treatment, aiming at the dissolution of the
771 island-like interlayer $\text{Ni}(\text{OH})_2$ layer, represents an easy and unambiguous way to
772 differentiate asbolane from todorokite which is unaffected by the treatment.

773 Both the presence of Co and Ni in synthesized phyllomanganates impede their
774 transformation to tectomanganates when refluxed, the origin of this similar impact
775 being different for the two metals, however. Oxidation of Co(II) sorbed on the MnO_2
776 layer and the subsequent structural incorporation of Co(III) in the octahedral layer
777 releases the steric strains related to the presence of Jahn-Teller distorted Mn(III)
778 octahedra, which is required for the phyllomanganate-to-tectomanganate conversion.
779 In contrast, the presence of hydrated Ni(II) favors the polymerization of fragments of
780 $\text{Ni}(\text{OH})_2$ octahedral layers, that in turn prevents the formation of tectomanganates
781 despite the favorable presence of Mn(III) in the octahedral MnO_2 layer. In both cases,
782 “foreign” metal cations are retained in the refluxed products, with contrasting ratios of
783 structural incorporation.

784

785 **ACKNOWLEDGMENTS**

786

787 Caroline Peacock (Leeds University, UK) is thanked for providing Ni K-edge
788 EXAFS data of Bir-Ni_S and Bir-Ni_V references. The authors are grateful to
789 Mengqiang Zhu (University of Wyoming, Laramie, Wy, USA) for helping collect
790 high-energy X-ray scattering data and providing Ni(II)-H₂O EXAFS reference. This
791 work is supported by the National Key Research and Development Program of China
792 (No. 2016YFD0800400) and the Natural Science Foundations of China (No.
793 41571448). Xionghan Feng, Bruno Lanson, and Zhongkuan Wu are supported by a
794 Cai Yuanpei program between the Key Laboratory of Arable Land Conservation
795 (Wuhan, China) and ISTerre (Grenoble, France)

796

REFERENCES

797

798

- 799 Atkins A.L., Shaw S. and Peacock C.L. (2014) Nucleation and growth of todorokite from
800 birnessite: Implications for trace-metal cycling in marine sediments. *Geochim. Cosmochim.*
801 *Acta* **144**, 109-125.
- 802 Atkins A.L., Shaw S. and Peacock C.L. (2016) Release of Ni from birnessite during transformation of
803 birnessite to todorokite: Implications for Ni cycling in marine sediments. *Geochim. Cosmochim.*
804 *Acta* **189**, 158-183.
- 805 Bish D.L. and Post J.E. (1989) Thermal behavior of complex, tunnel-structure manganese oxides. *Amer.*
806 *Mineral.* **74**, 177-186.
- 807 Bodei S., Manceau A., Geoffroy N., Baronnet A. and Buatier M. (2007) Formation of todorokite from
808 vernadite in Ni-rich hemipelagic sediments. *Geochim. Cosmochim. Acta* **71**, 5698-5716.
- 809 Burlet C. and Vanbrabant Y. (2015) Study of the spectro-chemical signatures of cobalt-manganese
810 layered oxides (asbolane-lithiophorite and their intermediates) by Raman spectroscopy. *J. Raman*
811 *Spectr.* **46**, 941-952.
- 812 Burns R.G., Burns V.M. and Stockman H.W. (1983) A review of the todorokite-buserite problem;
813 implications to the mineralogy of marine manganese nodules. *Amer. Mineral.* **68**, 972-980.
- 814 Ching S., Krukowska K.S. and Suib S.L. (1999) A new synthetic route to todorokite-type manganese
815 oxides. *Inorg. Chim. Acta* **294**, 123-132.
- 816 Chukhrov F.V. (1982) Crystallochemical nature of Co-Ni asbolan. *Int. Geol. Rev.* **24**, 598-604.
- 817 Chukhrov F.V., Drits V.A. and Gorshkov A.I. (1987) Structural Transformations of Manganese Oxides
818 in Oceanic Nodules. *Int. Geol. Rev.* **29**, 110-121.
- 819 Cui H.J., Liu X.W., Tan W.F., Feng X.H., Liu F. and Ruan H.D. (2008) Influence of Mn(III) availability
820 on the phase transformation from layered buserite to tunnel-structured todorokite. *Clay Clay Miner.*
821 **56**, 397-403.
- 822 Drits V.A., Lanson B., Gorshkov A.I. and Manceau A. (1998) Substructure and superstructure of
823 four-layer Ca-exchanged birnessite. *Amer. Mineral.* **83**, 97-118.
- 824 Drits V.A., Silvester E., Gorshkov A.I. and Manceau A. (1997) Structure of synthetic monoclinic
825 Na-rich birnessite and hexagonal birnessite: I. Results from X-ray diffraction and selected-area
826 electron diffraction. *Amer. Mineral.* **82**, 946-961.
- 827 Duff M.C., Hunter D.B., Triay I.R., Bertsch P.M., Reed D.T., Sutton S.R., Shea-McCarthy G., Kitten J.,
828 Eng P. and Chipera S.J. (1999) Mineral associations and average oxidation states of sorbed Pu on
829 tuff. *Environ. Sci. Technol.* **33**, 2163-2169.
- 830 Fan R. and Gerson A.R. (2015) Synchrotron micro-spectroscopic examination of Indonesian nickel
831 laterites. *Amer. Mineral.* **100**, 926-934.
- 832 Feitknecht W., Christen H.R. and Studer H., Z. (1956) Zur Kenntnis der höhern Nickelhydroxyde; die
833 Oxydation von Nickelhydroxyd. *Z. Anorg. Chem.* **283**, 88-95 (in German).
- 834 Feng Q., Xu Y., Kajiyoshi K. and Yanagisawa K. (2001) Hydrothermal Soft Chemical Synthesis of
835 Ni(OH)₂-Birnessite Sandwich Layered Compound and Layered LiNi_{1/3}Mn_{2/3}O₂. *Chem. Lett.* **30**,
836 1036-1037.
- 837 Feng X.H., Tan W.F., Liu F., Wang J.B. and Ruan H.D. (2004) Synthesis of todorokite at atmospheric
838 pressure. *Chem. Mater.* **16**, 4330-4336.

839 Feng X.H., Zhu M., Ginder-Vogel M., Ni C., Parikh S.J. and Sparks D.L. (2010) Formation of
840 nano-crystalline todorokite from biogenic Mn oxides. *Geochim. Cosmochim. Acta* **74**, 3232-3245.

841 Fuertes A., Da Costa-Serra J.F. and Chica A. (2012) New Catalysts based on Ni-Birnessite and
842 Ni-Todorokite for the Efficient Production of Hydrogen by Bioethanol Steam Reforming. *Energ.*
843 *Proc.* **29**, 181-191.

844 Gaillot A.-C., Drits V.A., Manceau A. and Lanson B. (2007) Structure of the synthetic K-rich
845 phyllosmanganate birnessite obtained by high-temperature decomposition of KMnO_4 . *Micropor.*
846 *Mesopor. Mater.* **98**, 267-282.

847 Gaillot A.-C., Flot D., Drits V.A., Manceau A., Burghammer M. and Lanson B. (2003) Structure of
848 synthetic K-rich birnessite obtained by high-temperature decomposition of KMnO_4 . I. Two-layer
849 polytype from 800 C experiment. *Chem. Mater.* **15**, 4666-4678.

850 Golden D.C., Chen C.C. and Dixon J.B. (1986) Synthesis of todorokite. *Science* **231**, 717-719.

851 Golden D.C., Chen C.C. and Dixon J.B. (1987) Transformation of birnessite to busserite, todorokite, and
852 manganite under mild hydrothermal treatment. *Clay Clay Miner.* **35**, 271-280.

853 Grangeon S., Fernandez-Martinez A., Claret F., Marty N., Tournassat C., Warmont F. and Gloter A.
854 (2017) In-situ determination of the kinetics and mechanisms of nickel adsorption by nanocrystalline
855 vernadite. *Chem. Geol.* **459**, 24-31.

856 Grangeon S., Fernandez-Martinez A., Warmont F., Gloter A., Marty N., Poulain A. and Lanson B.
857 (2015) Cryptomelane formation from nanocrystalline vernadite precursor: a high energy X-ray
858 scattering and transmission electron microscopy perspective on reaction mechanisms. *Geochem.*
859 *Trans.* **16**, 12.

860 Grangeon S., Lanson B. and Lanson M. (2014) Solid-state transformation of nanocrystalline
861 phyllosmanganate into tectomanganate: influence of initial layer and interlayer structure. *Acta*
862 *Crysrtallogr. B* **70**, 828-838.

863 Grangeon S., Lanson B., Lanson M. and Manceau A. (2008) Crystal structure of Ni-sorbed synthetic
864 vernadite: a powder X-ray diffraction study. *Mineral. Mag.* **72**, 1279-1291.

865 Hall D.S., Lockwood D.J., Bock C. and MacDougall B.R. (2015) Nickel hydroxides and related
866 materials: a review of their structures, synthesis and properties. *Proc. R. Soc. A* **471**, 20140792.

867 Johnson E.A. and Post J.E. (2006) Water in the interlayer region of birnessite: Importance in cation
868 exchange and structural stability. *Amer. Mineral.* **91**, 609-618.

869 Julien C.M., Massot M. and Poinssignon C. (2004) Lattice vibrations of manganese oxides. *Spectroc.*
870 *Acta Pt. A-Molec. Biomolec. Spectr.* **60**, 689-700.

871 Kasten S., Glasby G.P., Schulz H.D., Friedrich G. and Andreev S.I. (1998) Rare earth elements in
872 manganese nodules from the South Atlantic Ocean as indicators of oceanic bottom water flow. *Mar.*
873 *Geol.* **146**, 33-52.

874 Kwon K.D., Refson K. and Sposito G. (2013) Understanding the trends in transition metal sorption by
875 vacancy sites in birnessite. *Geochim. Cosmochim. Acta* **101**, 222-232.

876 Lanson B., Drits V.A., Feng Q. and Manceau A. (2002b) Structure of synthetic Na-birnessite: Evidence
877 for a triclinic one-layer unit cell. *Amer. Mineral.* **87**, 1662-1671.

878 Lanson B., Drits V.A., Gaillot A.-C., Silvester E., Plançon A. and Manceau A. (2002a) Structure of
879 heavy-metal sorbed birnessite: Part 1. Results from X-ray diffraction. *Amer. Mineral.* **87**,
880 1631-1645.

881 Lanson B., Drits V.A., Silvester E. and Manceau A. (2000) Structure of H-exchanged hexagonal
882 birnessite and its mechanism of formation from Na-rich monoclinic busserite at low pH. *Amer.*

883 *Mineral.* **85**, 826-838.

884 Lanson B., Marcus M.A., Fakra S., Panfili F., Geoffroy N. and Manceau A. (2008) Formation of Zn–Ca
885 phylломanganate nanoparticles in grass roots. *Geochim. Cosmochim. Acta* **72**, 2478-2490.

886 Lefkowitz J.P. and Elzinga E.J. (2017) Structural alteration of hexagonal birnessite by aqueous Mn(II):
887 Impacts on Ni(II) sorption. *Chem. Geol.* **466**, 524-532.

888 Li W., Harrington R., Tang Y., Kubicki J.D., Aryanpour M., Reeder R.J., Parise J.B. and Phillips B.L.
889 (2011) Differential pair distribution function study of the structure of arsenate adsorbed on
890 nanocrystalline γ -alumina. *Environ. Sci. Technol.* **45**, 9687-9692.

891 Li Y.F., Zhu S.C. and Liu Z.P. (2016) Reaction Network of Layer-to-Tunnel Transition of MnO₂. *J. Am.*
892 *Chem. Soc.* **138**, 5371-5379.

893 Llorca S. (1988) Nouvelles données sur la composition et la structure des asbolanes
894 (Nouvelle-Calédonie). *C. R. Acad. Sci Paris - Série II* **307**, 155-161.

895 Luo J., Zhang Q., Huang A., Giraldo O. and Suib S.L. (1999) Double-aging method for preparation of
896 stabilized Na– buserite and transformations to todorokites incorporated with various metals. *Inorg.*
897 *Chem.* **38**, 6106-6113.

898 Manceau A., Gorshkov A.I. and Drits V.A. (1992a) Structural chemistry of Mn, Co, and Ni in
899 manganese hydrous oxides. I. Information from EXAFS spectroscopy and electron and X-ray
900 diffraction. *Amer. Mineral.* **77**, 1144-1157.

901 Manceau A., Gorshkov A.I. and Drits V.A. (1992b) Structural chemistry of Mn, Co, and Ni in
902 manganese hydrous oxides. I. Information from XANES spectroscopy. *Amer. Mineral.* **77**,
903 1133-1143.

904 Manceau A., Kersten M., Marcus M.A., Geoffroy N. and Granina L. (2007a) Ba and Ni speciation in a
905 nodule of binary Mn oxide phase composition from Lake Baikal. *Geochim. Cosmochim. Acta* **71**,
906 1967-1981.

907 Manceau A., Lanson M. and Geoffroy N. (2007b) Natural speciation of Ni, Zn, Ba, and As in
908 ferromanganese coatings on quartz using X-ray fluorescence, absorption, and diffraction. *Geochim.*
909 *Cosmochim. Acta* **71**, 95-128.

910 Manceau A., Lanson M. and Takahashi Y. (2014) Mineralogy and crystal chemistry of Mn, Fe, Co, Ni,
911 and Cu in a deep-sea Pacific polymetallic nodule. *Amer. Mineral.* **99**, 2068-2083.

912 Manceau A., Llorca S. and Calas G. (1987) Crystal chemistry of cobalt and nickel in lithiophorite and
913 asbolane from New Caledonia. *Geochim. Cosmochim. Acta* **51**, 105-113.

914 Manceau A., Marcus M.A. and Grangeon S. (2012) Determination of Mn valence states in
915 mixed-valent manganates by XANES spectroscopy. *Amer. Mineral.* **97**, 816-827.

916 Manceau A., Silvester E., Bartoli C., Lanson B. and Drits V.A. (1997) Structural mechanism of Co²⁺
917 oxidation by the phylломanganate buserite. *Amer. Mineral.* **82**, 1150-1175.

918 Manceau A., Tamura N., Marcus M.A., MacDowell A.A., Celestre R.S., Sublett R.E., Sposito G. and
919 Padmore H.A. (2002) Deciphering Ni sequestration in soil ferromanganese nodules by combining
920 X-ray fluorescence, absorption, and diffraction at micrometer scales of resolution. *Amer. Mineral.*
921 **87**, 1494-1499.

922 Marcus M.A., Manceau A. and Kersten M. (2004) Mn, Fe, Zn and As speciation in a fast-growing
923 ferromanganese marine nodule. *Geochim. Cosmochim. Acta* **68**, 3125-3136.

924 Nicolas-Tolentino E., Tian Z.-R., Zhou H., Xia G. and Suib S.L. (1999) Effects of Cu²⁺ ions on the
925 structure and reactivity of todorokite-and cryptomelane-type manganese oxide octahedral molecular
926 sieves. *Chem. Mater.* **11**, 1733-1741.

927 Ohnuki T., Jiang M., Sakamoto F., Kozai N., Yamasaki S., Yu Q., Tanaka K., Utsunomiya S., Xia X.,
928 Yang K. and He J. (2015) Sorption of trivalent cerium by a mixture of microbial cells and
929 manganese oxides: Effect of microbial cells on the oxidation of trivalent cerium. *Geochim.*
930 *Cosmochim. Acta* **163**, 1-13.

931 Ohta A. and Kawabe I. (2001) REE(III) adsorption onto Mn dioxide (δ -MnO₂) and Fe
932 oxyhydroxide: Ce(III) oxidation by δ -MnO₂. *Geochim. Cosmochim. Acta* **65**, 695-703.

933 Onda A., Hara S., Kajiyoshi K. and Yanagisawa K. (2007) Synthesis of manganese oxide octahedral
934 molecular sieves containing cobalt, nickel, or magnesium, and the catalytic properties for hydration
935 of acrylonitrile. *Appl. Catal. A. Gen.* **321**, 71-78.

936 Peacock C.L. (2009) Physiochemical controls on the crystal-chemistry of Ni in birnessite: Genetic
937 implications for ferromanganese precipitates. *Geochim. Cosmochim. Acta* **73**, 3568-3578.

938 Peacock C.L. and Sherman D.M. (2007a) Crystal-chemistry of Ni in marine ferromanganese crusts and
939 nodules. *Amer. Mineral.* **92**, 1087-1092.

940 Peacock C.L. and Sherman D.M. (2007b) Sorption of Ni by birnessite: Equilibrium controls on Ni in
941 seawater. *Chem. Geol.* **238**, 94-106.

942 Peña J., Kwon K.D., Refson K., Bargar J.R. and Sposito G. (2010) Mechanisms of nickel sorption by a
943 bacteriogenic birnessite. *Geochim. Cosmochim. Acta* **74**, 3076-3089.

944 Ploquin F., Fritsch E., Guigner J.M., Esteve I., Delbes L., Dublet G. and Juillot F. (2018)
945 Phyllo-manganate vein-infillings in faulted and Al-poor regoliths of the New Caledonian ophiolite:
946 periodic and sequential crystallization of Ni-asbolane, Alk-birnessite and H-birnessite. *Eur. J.*
947 *Mineral.*

948 Post J.E. (1999) Manganese oxide minerals: Crystal structures and economic and environmental
949 significance. *Proc. Nat. Acad. Sci.* **96**, 3447-3454

950 Post J.E. and Bish D.L. (1988) Rietveld refinement of the todorokite structure. *Amer. Mineral.* **73**,
951 861-869.

952 Post J.E., Heaney P.J. and Hanson J. (2003) Synchrotron X-ray diffraction study of the structure and
953 dehydration behavior of todorokite. *Amer. Mineral.* **88**, 142-150.

954 Qin Z., Yin H., Wang X., Zhang Q., Lan S., Koopal L.K., Zheng L., Feng X. and Liu F. (2018) The
955 preferential retention of ^{VI}Zn over ^{IV}Zn on birnessite during dissolution/desorption. *Appl. Clay Sci.*
956 **161**, 169-175.

957 Ravel B. and Newville M. (2005) ATHENA and ARTEMIS: interactive graphical data analysis using
958 IFEFFIT. *Phys. Scripta* **2005**, 1007.

959 Remucal C.K. and Ginder-Vogel M. (2014) A critical review of the reactivity of manganese oxides with
960 organic contaminants. *Envir. Sci.-Proc. Imp.* **16**, 1247-1266.

961 Roque-Rosell J., Mosselmans J.F.W., Proenza J.A., Labrador M., Gali S., Atkinson K.D. and Quinn P.D.
962 (2010) Sorption of Ni by "lithiophorite-asbolane" intermediates in Moa Bay lateritic deposits,
963 eastern Cuba. *Chem. Geol.* **275**, 9-18.

964 Shen X., Morey A.M., Liu J., Ding Y., Cai J., Durand J., Wang Q., Wen W., Hines W.A., Hanson J.C.,
965 Bai J., Frenkel A.I., Reiff W., Aindow M. and Suib S.L. (2011) Characterization of the Fe-Doped
966 Mixed-Valent Tunnel Structure Manganese Oxide KOMS-2. *J. Phys. Chem. C* **115**, 21610-21619.

967 Shen Y.-F., Suib S.L. and O'Young C.-L. (1994) Effects of inorganic cation templates on octahedral
968 molecular sieves of manganese oxide. *J. Am. Chem. Soc.* **116**, 11020-11029.

969 Shen Y.F., Zenger R.P., DeGuzman R.N., Suib S.L., McCurdy L., Potter D.I. and O'Young C.L. (1993)
970 Manganese oxide octahedral molecular sieves: preparation, characterization, and applications.

971 *Science* **260**, 511-515.

972 Sherman D.M. and Peacock C.L. (2010) Surface complexation of Cu on birnessite (δ -MnO₂): Controls
973 on Cu in the deep ocean. *Geochim. Cosmochim. Acta* **74**, 6721-6730.

974 Siegel M.D. and Turner S. (1983) Crystalline todorokite associated with biogenic debris in manganese
975 nodules. *Science* **219**, 172-174.

976 Simanova A.A., Kwon K.D., Bone S.E., Bargar J.R., Refson K., Sposito G. and Peña J. (2015) Probing
977 the sorption reactivity of the edge surfaces in birnessite nanoparticles using nickel(II). *Geochim.
978 Cosmochim. Acta* **164**, 191-204.

979 Simanova A.A. and Pena J. (2015) Time-Resolved Investigation of Cobalt Oxidation by Mn(III)-Rich
980 δ -MnO₂ Using Quick X-ray Absorption Spectroscopy. *Environ. Sci. Technol.* **49**, 10867-10876.

981 Smith D.W. (1977) Ionic hydration enthalpies. *J. Chem. Educ.* **54**, 540.

982 Song C., Li R., Liu F., Feng X., Tan W. and Qiu G. (2010) Cobalt-doped todorokites prepared by
983 refluxing at atmospheric pressure as cathode materials for Li batteries. *Electrochim. Acta* **55**,
984 9157-9165.

985 Spinks S.C., Uvarova Y., Thorne R., Anand R., Reid N., White A., Ley-Cooper Y., Bardwell N., Gray
986 D., Meadows H. and LeGras M. (2017) Detection of zinc deposits using terrestrial ferromanganese
987 crusts. *Ore Geol. Rev.* **80**, 484-503.

988 Tian Z.-R., Yin Y.-G., Suib S.L. and O'Young C.L. (1997) Effect of Mg²⁺ ions on the formation of
989 todorokite type manganese oxide octahedral molecular sieves. *Chem. Mater.* **9**, 1126-1133.

990 Toner B., Manceau A., Webb S.M. and Sposito G. (2006) Zinc sorption to biogenic
991 hexagonal-birnessite particles within a hydrated bacterial biofilm. *Geochim. Cosmochim. Acta* **70**,
992 27-43.

993 Turner S. and Buseck P.R. (1981) Todorokites: A new family of naturally occurring manganese oxides.
994 *Science* **212**, 1024-1027.

995 Wang X., Li W., Harrington R., Liu F., Parise J.B., Feng X. and Sparks D.L. (2013) Effect of
996 ferrihydrite crystallite size on phosphate adsorption reactivity. *Environ. Sci. Technol.* **47**,
997 10322-10331.

998 Wang Z., Lv K., Wang G., Deng K. and Tang D. (2010) Study on the shape control and photocatalytic
999 activity of high-energy anatase titania. *Appl. Catal. B. Environ.* **100**, 378-385.

1000 Webb S.M. (2005) Structural characterization of biogenic Mn oxides produced in seawater by the
1001 marine bacillus sp. strain SG-1. *Amer. Mineral.* **90**, 1342-1357.

1002 Wegorzewski A.V., Kuhn T., Dohrmann R., Wirth R. and Grangeon S. (2015) Mineralogical
1003 characterization of individual growth structures of Mn-nodules with different Ni+Cu content from
1004 the central Pacific Ocean. *Amer. Mineral.* **100**, 2497-2508.

1005 Wu Z., Peacock C.L., Lanson B., Yin H., Zheng L., Chen Z., Tan W., Qiu G., Liu F. and Feng X. (2019)
1006 Transformation of Co-containing birnessite to todorokite: Effect of Co on the transformation and
1007 implications for Co mobility. *Geochim. Cosmochim. Acta* **246**, 21-40.

1008 Xu H., Chen T. and Konishi H. (2010) HRTEM investigation of trilling todorokite and nano-phase
1009 Mn-oxides in manganese dendrites. *Amer. Mineral.* **95**, 556-562.

1010 Yang P., Lee S., Post J.E., Xu H.F., Wang Q., Xu W.Q. and Zhu M.Q. (2018) Trivalent manganese on
1011 vacancies triggers rapid transformation of layered to tunneled manganese oxides (TMOs):
1012 Implications for occurrence of TMOs in low-temperature environment. *Geochim. Cosmochim. Acta*
1013 **240**, 173-190.

1014 Yin H., Feng X., Qiu G., Tan W. and Liu F. (2011a) Characterization of Co-doped birnessites and

1015 application for removal of lead and arsenite. *J. Hazard. Mater.* **188**, 341-349.

1016 Yin H., Li H., Wang Y., Ginder-Vogel M., Qiu G., Feng X., Zheng L. and Liu F. (2014) Effects of Co
1017 and Ni co-doping on the structure and reactivity of hexagonal birnessite. *Chem. Geol.* **381**, 10-20.

1018 Yin H., Liu F., Feng X., Liu M., Tan W. and Qiu G. (2011b) Co²⁺-exchange mechanism of birnessite
1019 and its application for the removal of Pb²⁺ and As(III). *J. Hazard. Mater.* **196**, 318-326.

1020 Yin H., Liu Y., Koopal L.K., Feng X., Chu S., Zhu M. and Liu F. (2015) High Co-doping promotes the
1021 transition of birnessite layer symmetry from orthogonal to hexagonal. *Chem. Geol.* **410**, 12-20.

1022 Yin H., Tan W., Zheng L., Cui H., Qiu G., Liu F. and Feng X. (2012) Characterization of Ni-rich
1023 hexagonal birnessite and its geochemical effects on aqueous Pb²⁺/Zn²⁺ and As(III). *Geochim.
1024 Cosmochim. Acta* **93**, 47-62.

1025 Yu Q., Sasaki K., Tanaka K., Ohnuki T. and Hirajima T. (2012) Structural factors of biogenic birnessite
1026 produced by fungus *Paraconiothyrium* sp. WL-2 strain affecting sorption of Co²⁺. *Chem. Geol.*
1027 **310-311**, 106-113.

1028 Yu Q.Q., Sasaki K., Tanaka K., Ohnuki T. and Hirajima T. (2013) Zinc Sorption During Bio-oxidation
1029 and Precipitation of Manganese Modifies the Layer Stacking of Biogenic Birnessite. *Geomicrobiol.
1030 J.* **30**, 829-839.

1031 Zawadzki D., Maciag L., Kotlinski R.A., Kozub-Budzyn G.A., Piestrzynski A. and Wrobel R. (2018)
1032 Geochemistry of cobalt-rich ferromanganese crusts from the Perth Abyssal Plain (E Indian Ocean).
1033 *Ore Geol. Rev.* **101**, 520-531.

1034 Zhao H.Y., Liang X.R., Yin H., Liu F., Tan W.F., Qiu G.H. and Feng X.H. (2015) Formation of
1035 todorokite from "c-disordered" H⁺-birnessites: the roles of average manganese oxidation state and
1036 interlayer cations. *Geochem. Trans.* **16**, 11.

1037 Zhu M., Farrow C.L., Post J.E., Livi K.J.T., Billinge S.J.L., Ginder-Vogel M. and Sparks D.L. (2012)
1038 Structural study of biotic and abiotic poorly-crystalline manganese oxides using atomic pair
1039 distribution function analysis. *Geochim. Cosmochim. Acta* **81**, 39-55.

1040

1041
1042
1043

Table 1

Chemical composition and specific surface area of layered precursors and reflux products

Samples	Mn wt. %	Ni wt. %	Ni/(Mn+Ni) mol%	Mg wt. %	(Mg+Ni)/Mn mol%	SSA (m ² /g)
Bir	55.4(1.0)	--	--	--	--	--
NiB1	54.1(1.1)	0.39(1)	0.67	--	--	--
NiB5	53.7(1.0)	1.86(4)	3.18	--	--	--
NiB10	51.2(1.0)	3.89(7)	5.98	--	--	--
NiB15	47.3(1.7)	5.32(3)	8.71	--	--	--
NiB20	44.8(1.8)	7.14(7)	11.50	--	--	--
Tod	54.4(2.1)	--	--	3.95(8)	16.4	90.7
NiT1	54.3(8)	0.33(1)	0.57	3.51(12)	16.2	--
NiT5	54.2(6)	1.57(2)	2.57	3.12(2)	15.6	93.7
NiT10	52.7(6)	3.79(1)	5.94	2.61(2)	17.5	119.7
NiT15	52.4(1.2)	5.66(9)	8.41	2.59(6)	20.4	109.0
NiT20	49.2(9)	7.74(2)	11.38	2.11(2)	22.5	106.8

1044

1045 **Table 2.**

1046 Weight loss of layered precursors and reflux products over specific temperature
1047 intervals

Temperature (°C)	Weight loss/%				
	Bir	NiB5	NiB10	NiB15	NiB20
RT-100	2.45	2.87	2.64	2.84	9.25
100-170	8.43	7.14	6.54	5.73	4.87
170-400	1.78	4.10	4.74	5.78	6.72
Total	17.38	19.20	18.85	19.15	25.31
	Tod	NiT5	NiT10	NiT15	NiT20
RT-110	2.75	2.93	3.39	3.90	4.12
110-240	8.05	7.68	7.43	6.57	6.12
240-380	5.47	5.32	5.04	5.34	5.97
380-500	2.69	2.33	2.08	1.93	1.79
500-650	4.50	4.35	4.06	3.75	3.61
Total	23.47	22.61	22.01	21.48	21.60

1048

1049 **Table 3.**

1050 Fractional and average valence states of Mn obtained for layered precursors and
1051 reflux products from the Combo fit of XANES spectra and 1st derivatives. The
1052 estimated error for Combo method is $\pm 4\%$ (Manceau et al., 2012; Yin et al., 2015)

Sample	Mn ²⁺ at. %	Mn ³⁺ at. %	Mn ⁴⁺ at. %	Mn-AOS
Bir	3	26	72	3.69
NiB1	2	25	74	3.71
NiB5	2	30	67	3.64
NiB10	2	31	68	3.66
NiB15	0	31	69	3.69
NiB20	0	35	65	3.65
Tod	2	25	74	3.72
NiT1	1	35	65	3.64
NiT5	3	32	66	3.63
NiT10	2	35	64	3.62
NiT15	1	34	65	3.64
NiT20	0	33	67	3.67

1053

1054 **Figure Captions**

1055

1056 **Fig. 1.** XRD patterns of layered precursors (top) and reflux products (bottom). Colors
1057 correspond to the Ni/(Ni+Mn) ratio of the samples. Green ticks at the bottom of upper
1058 and lower figures indicate the reflections of triclinic birnessite (ICDD #43-1456) and
1059 todorokite (ICDD #38-0475), respectively.

1060

1061 **Fig. 2.** XRD patterns collected for NiT20, NiT15, and Tod at (a) Mn K-edge (6.5 keV),
1062 (b) Ni K-edge (8.3 eV), (c) 12.0 keV, and (d) 18.0 keV. Intensities were systematically
1063 normalized to the most intense reflection. Colors as in **Fig. 1.** (e) XRD patterns
1064 calculated for an asbolane containing 0.525 Ni(OH)₂ in MnO₂ interlayers. Contents of
1065 Ni and Mn atoms are reduced by 20% at their respective absorption edges to simulate
1066 the anomalous effect.

1067

1068 **Fig. 3.** FTIR spectra of layered precursors and reflux products (top and bottom,
1069 respectively). Colors as in **Fig. 1.**

1070

1071 **Fig. 4.** HRTEM images of (a-b): Tod, (c-e): NiT1, (f-h): NiT5, (i-m): NiT1. Numbers
1072 in (b) and (d) indicate the number of MnO₆ octahedra defining tunnel width. Arrows
1073 in (i) and (l) indicate the direction of fringes bending.

1074

1075 **Fig. 5.** Proportion of metal cations released during the nitric acid treatment: (a-b): Mn,
1076 (c-d): Ni, and (f): Mg. The amount of metal released is normalized to the sample
1077 overall metal content (see text for details). (e): XRD patterns of samples treated with
1078 nitric acid. Colors as in **Fig. 1** except for Bir in (e).

1079

1080 Fig. 6. Thermogravimetric analysis traces obtained for (a) layered precursors and (b)
1081 reflux products, and their 1st derivatives (c and d, respectively). 1st derivative curves
1082 were smoothed using a Savitzky-Golay filter and a 15 point window. Colors as in Fig.
1083 1.

1085 Fig. 7. XPS O1s spectra obtained for layered precursors and reflux products (left and
1086 right, respectively). The thick solid curve represents the best fit to the data (open red
1087 squares). Peaks corresponding to O²⁻, OH⁻, and H₂O species are shown in the order of
1088 increasing binding energy as dashed purple, dotted-dashed green, and dotted blue
1089 lines, respectively. The green dotted line is the difference curve.

1091 Fig. 8. Mn K-edge EXAFS spectra obtained for (a) layered precursors and (b) reflux
1092 products. Colors as in Fig. 1.

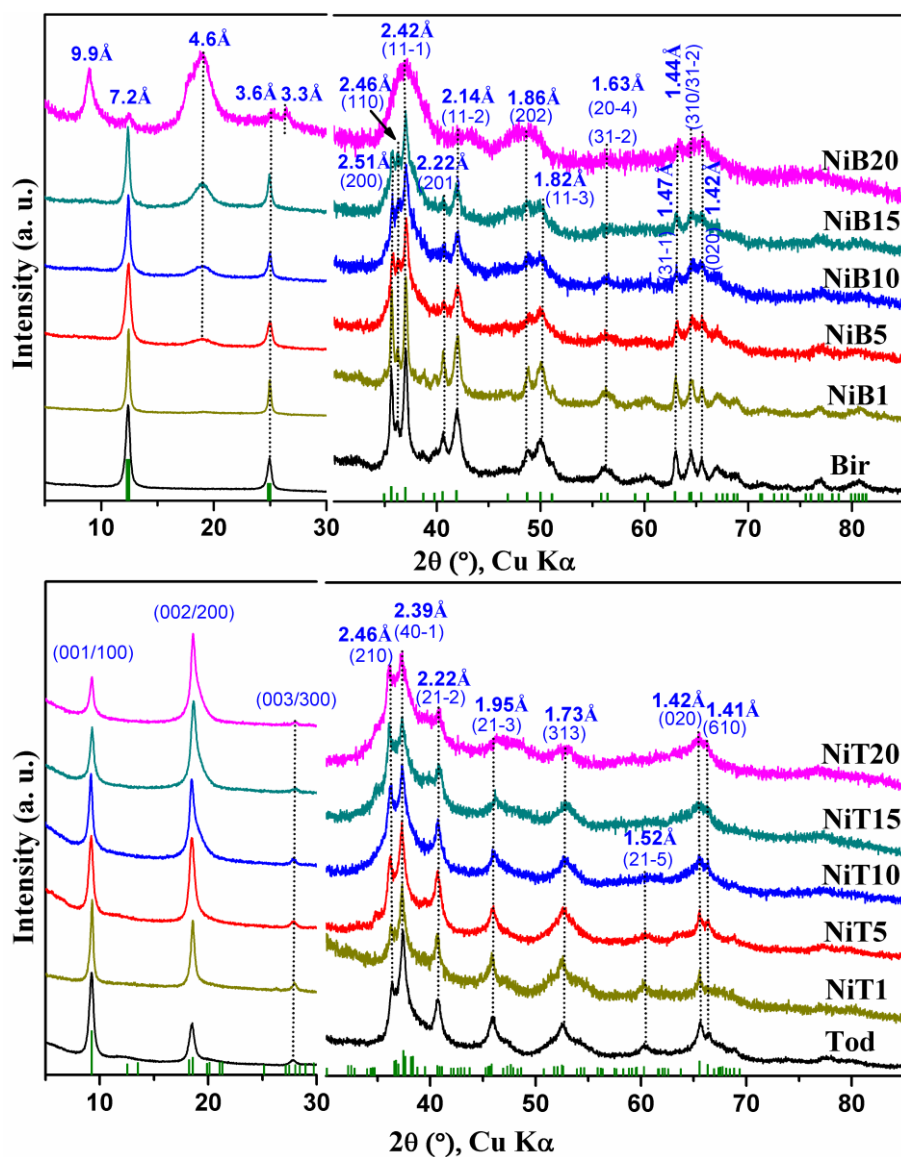
1094 Fig. 9. Comparison of (a, c) Mn K-edge EXAFS and (b, d) of their FTs (showing both
1095 real and imaginary parts) obtained for Ni-rich (Top: NiB15 and NiT15) and Ni-free
1096 (bottom: Bir and Tod) layered precursors and corresponding reflux products.

1098 Fig. 10. Comparison of Ni K-edge EXAFS spectra obtained for layered precursors
1099 and reflux products with reference spectra. Sample colors as in Fig. 1.

1101 Fig. 11. Pair distribution functions obtained for Ni-rich (NiT10 and NiT20) and
1102 Ni-free (Tod) reflux products (top). Middle: d-PDFs relative to Tod PDF data; bottom:
1103 PDFs calculated for Ni (hydr)oxides (ICSD #76670 and #28101 for NiO and Ni(OH)₂,
1104 respectively). Intensities of experimental PDFs and of difference PDFs were
1105 normalized to the 2.9-3.1 Å peak.

1106

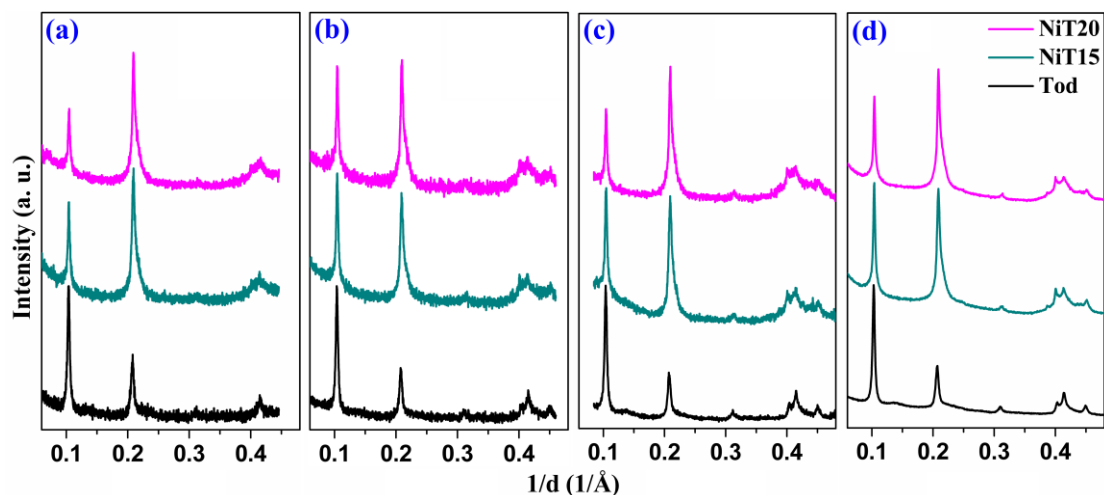
1107 **Fig. 12.** Intensity distributions calculated for ideal todorokite (ICDD #38-0475) with
1108 (a) only Mg in todorokite tunnels and (b) with Mg and Ni present in a 1:1 ratio in
1109 todorokite tunnels. In both cases, the model of Post et al. (2003) was modified
1110 assuming the complete filling of the O8 site by H₂O molecules (no cations) and the
1111 presence of 1.0 cation (Mg or Mg+Ni) in the Mg site.



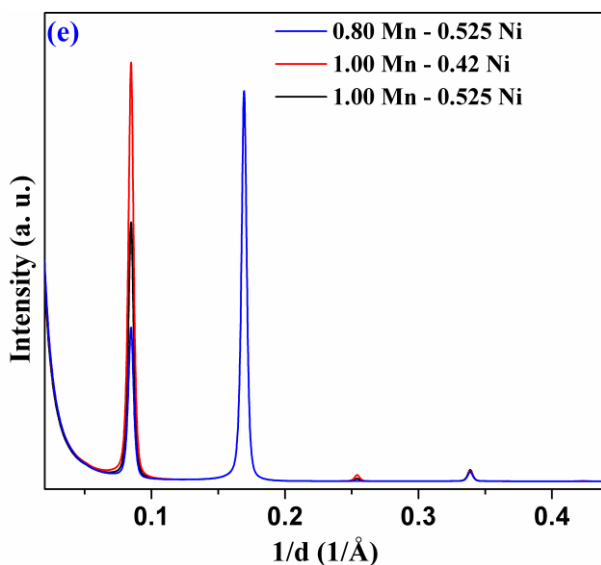
1

2 **Fig. 1.** XRD patterns of layered precursors (top) and reflux products (bottom). Colors
 3 correspond to the Ni/(Ni+Mn) ratio of the samples. Green ticks at the bottom of upper
 4 and lower figures indicate the reflections of triclinic birnessite (ICDD #43-1456) and
 5 todorokite (ICDD #38-0475), respectively.

6

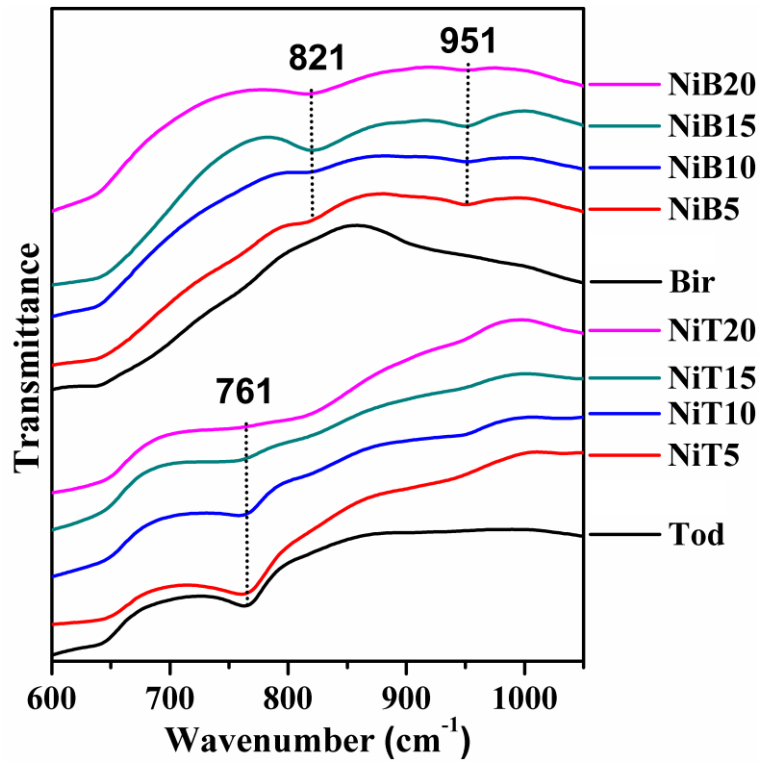


7



8

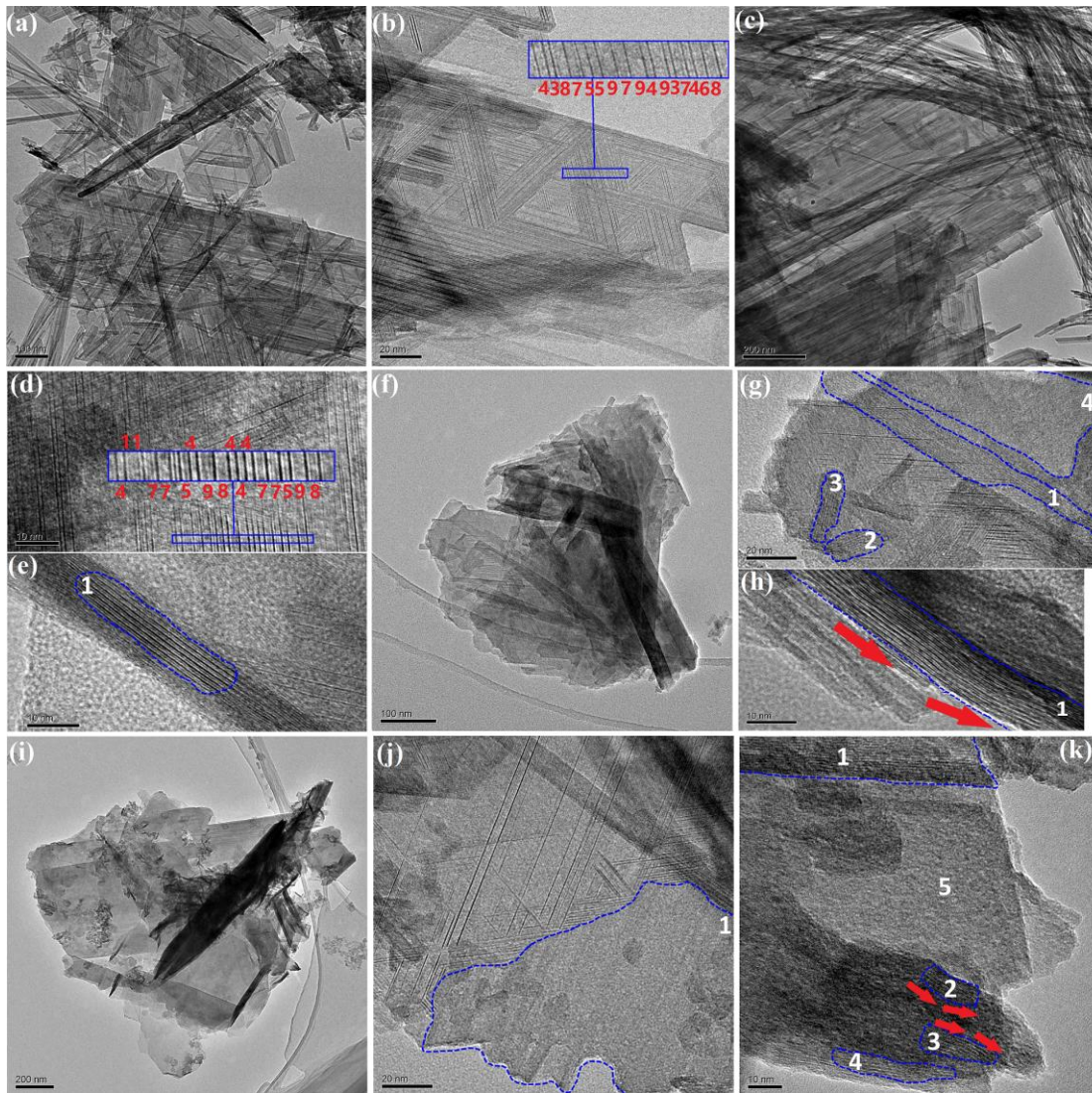
9 **Fig. 2.** XRD patterns collected for NiT20, NiT15, and Tod at (a) Mn K-edge (6.5 keV),
 10 (b) Ni K-edge (8.3 eV), (c) 12.0 keV, and (d) 18.0 keV. Intensities were systematically
 11 normalized to the most intense reflection. Colors as in **Fig. 1.** (e) XRD patterns
 12 calculated for an asbolane containing 0.525 $\text{Ni}(\text{OH})_2$ in MnO_2 interlayers. Contents of
 13 Ni and Mn atoms are reduced by 20% at their respective absorption edges to simulate
 14 the anomalous effect.
 15



16

17 **Fig. 3.** FTIR spectra of layered precursors and reflux products (top and bottom,
 18 respectively). Colors as in **Fig. 1.**

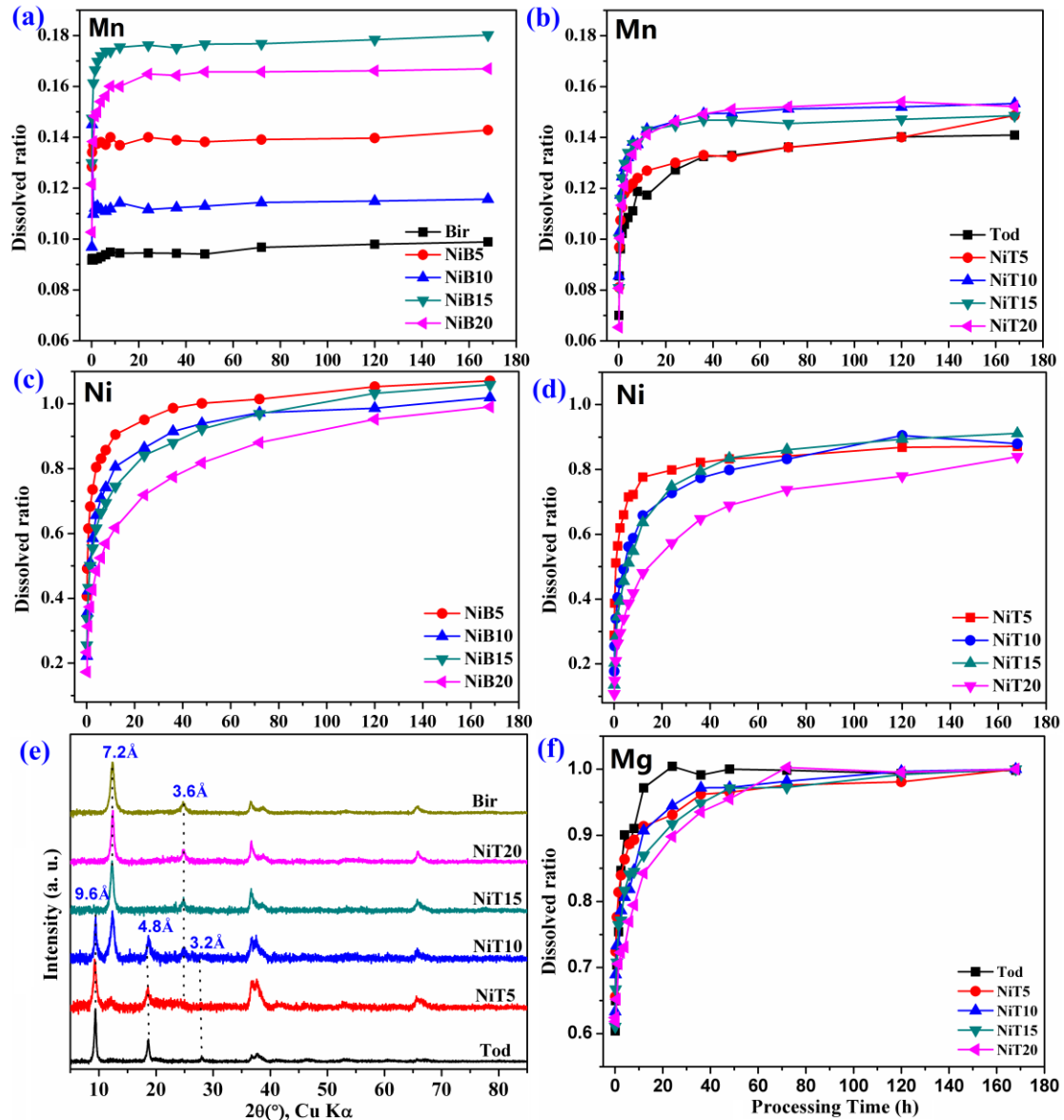
19



20

21 **Fig. 4.** HRTEM images of (a-b): Tod, (c-e): NiT1, (f-h): NiT5, (i-m): NiT1. Numbers
 22 in (b) and (d) indicate the number of MnO₆ octahedra defining tunnel width. Arrows
 23 in (i) and (l) indicate the direction of fringes bending.

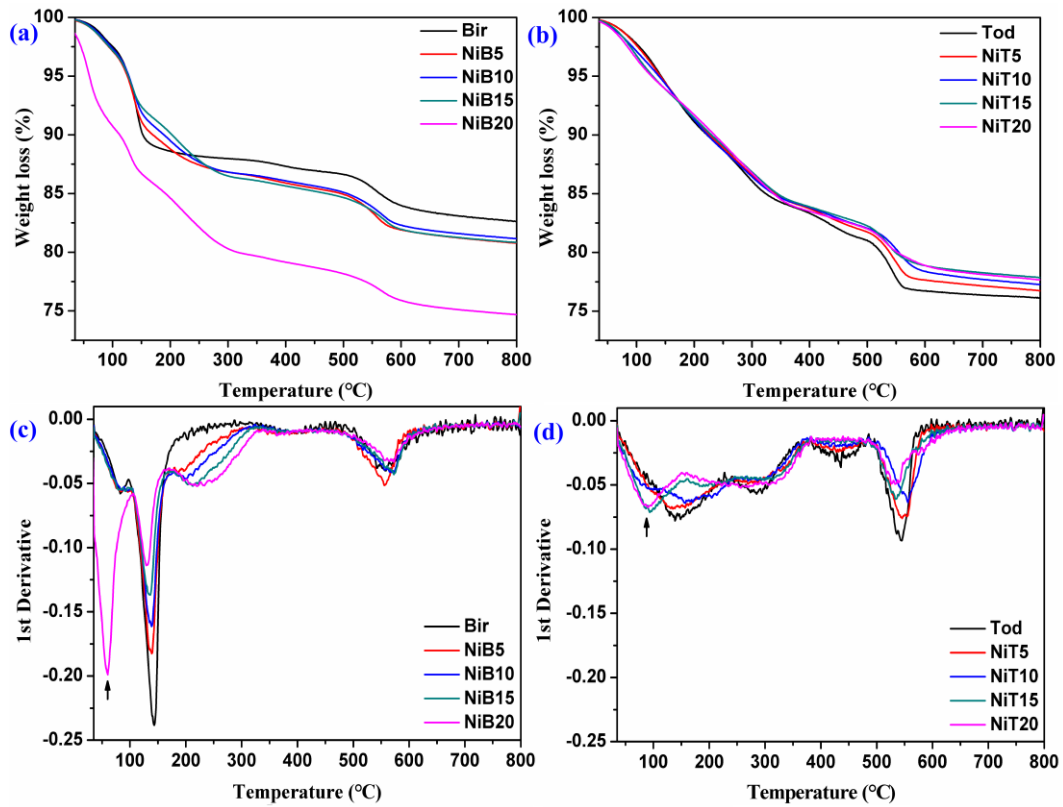
24



25

26 **Fig. 5.** Proportion of metal cations released during the nitric acid treatment: (a-b): Mn,
 27 (c-d): Ni, and (f): Mg. The amount of metal released is normalized to the sample
 28 overall metal content (see text for details). (e): XRD patterns of samples treated with
 29 nitric acid. Colors as in **Fig. 1** except for Bir in (e).

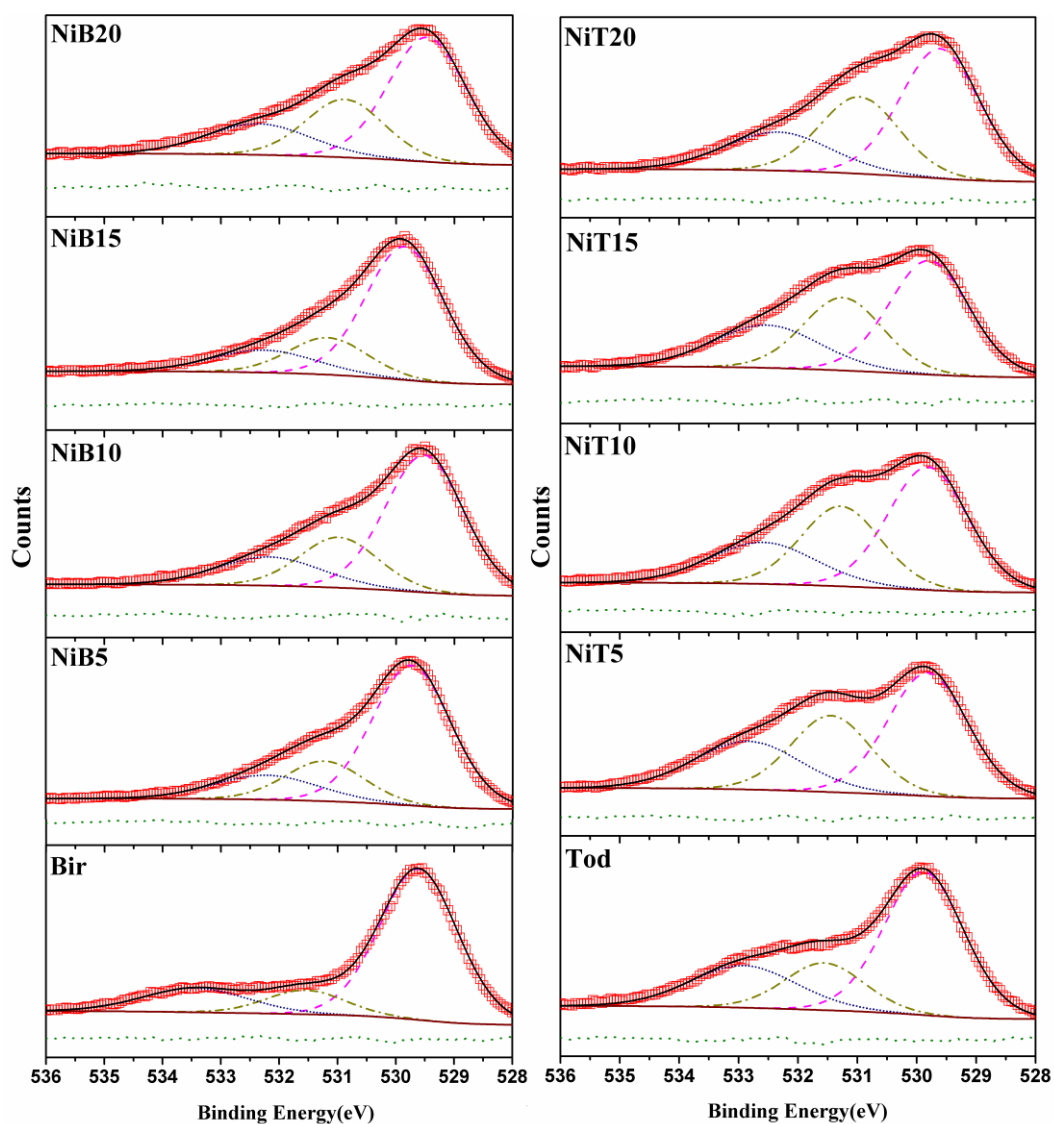
30



31

32 **Fig. 6.** Thermogravimetric analysis traces obtained for (a) layered precursors and (b)
 33 reflux products, and their 1st derivatives (c and d, respectively). 1st derivative curves
 34 were smoothed using a Savitzky-Golay filter and a 15 points window. Colors as in **Fig.**
 35 **1.**

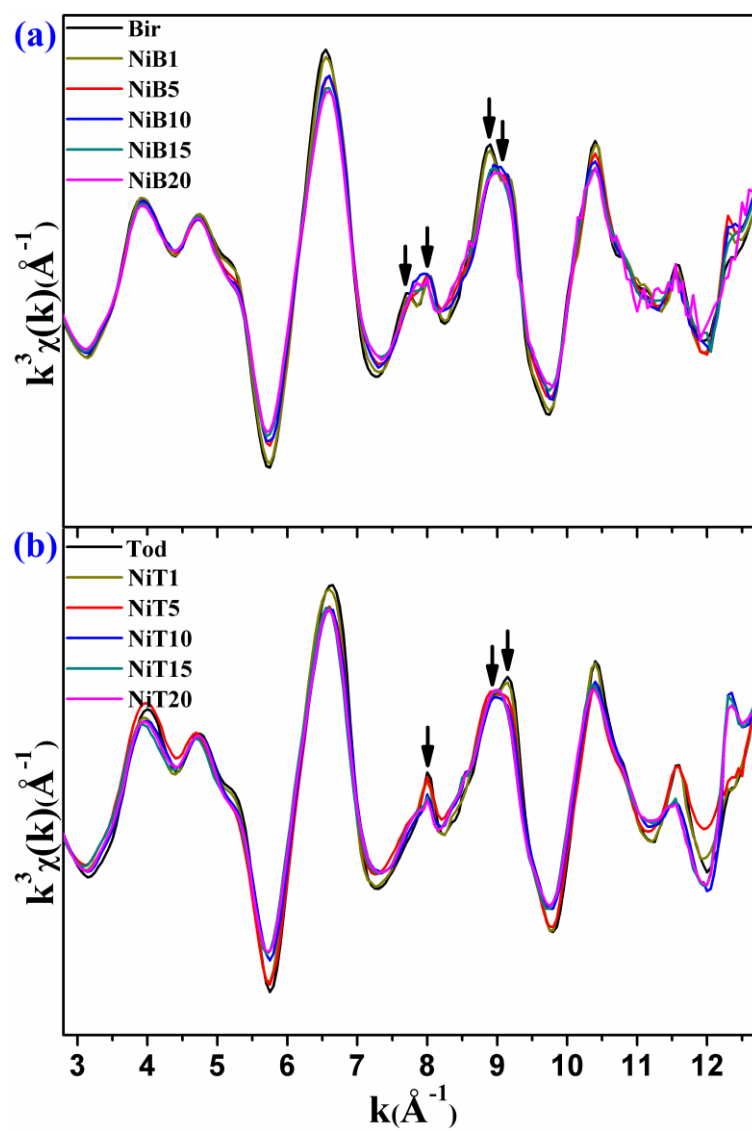
36



37

38 **Fig. 7.** XPS O1s spectra obtained for layered precursors and reflux products (left and
 39 right, respectively). The thick solid curve represents the best fit to the data (open red
 40 squares). Peaks corresponding to O^{2-} , OH^- , and H_2O species are shown in the order of
 41 increasing binding energy as dashed purple, dotted-dashed green, and dotted blue
 42 lines, respectively. The green dotted line is the difference curve.

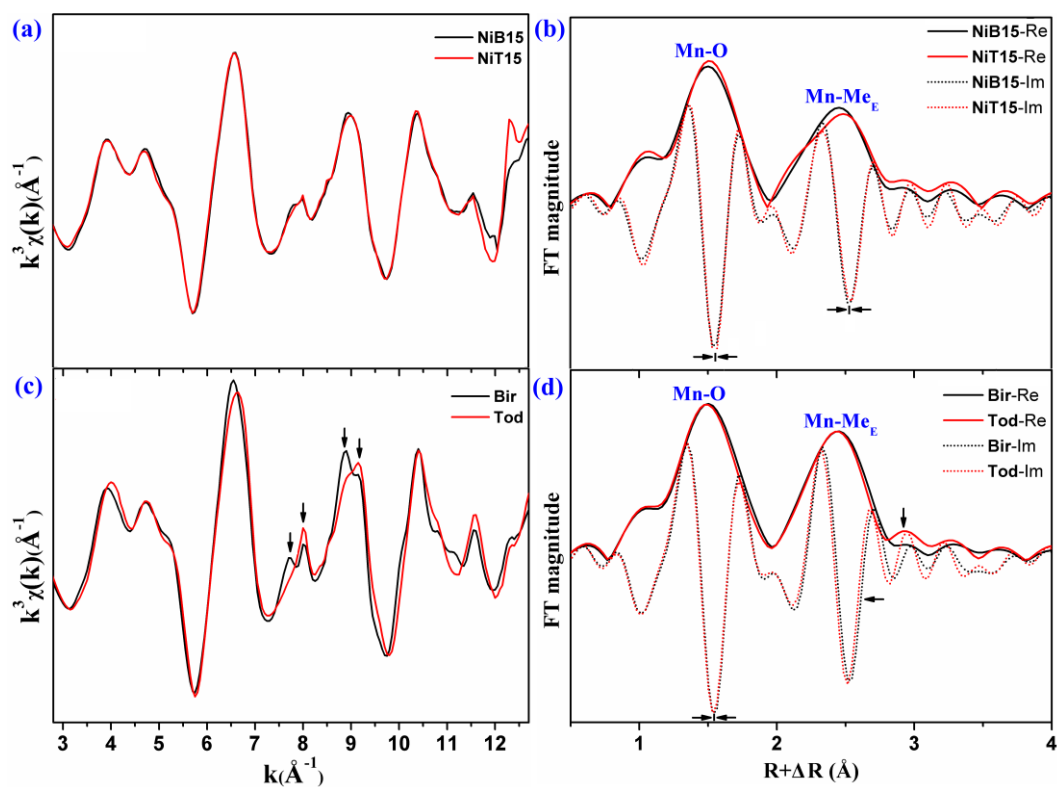
43



44

45 **Fig. 8.** Mn K-edge EXAFS spectra obtained for (a) layered precursors and (b) reflux
 46 products. Colors as in **Fig. 1.**

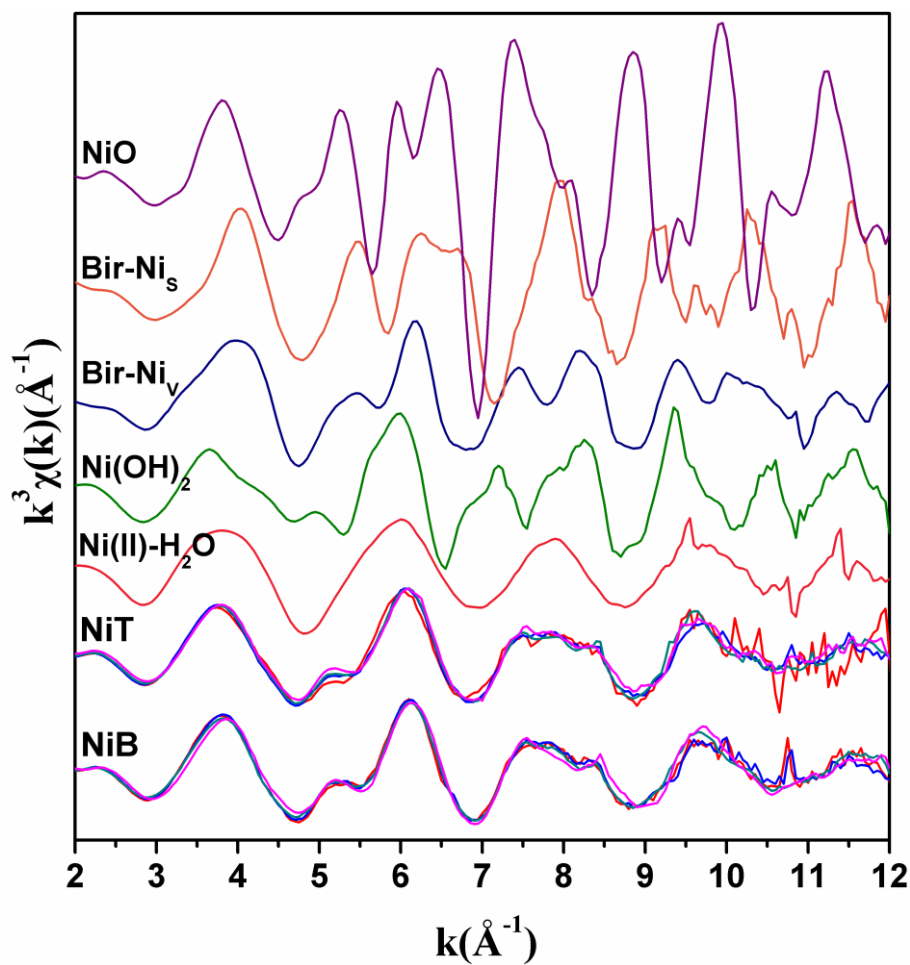
47



48

49 **Fig. 9.** Comparison of (a, c) Mn K-edge EXAFS and (b, d) of their FTs (showing both
 50 real and imaginary parts) obtained for Ni-rich (Top: NiB15 and NiT15) and Ni-free
 51 (bottom: Bir and Tod) layered precursors and corresponding reflux products.

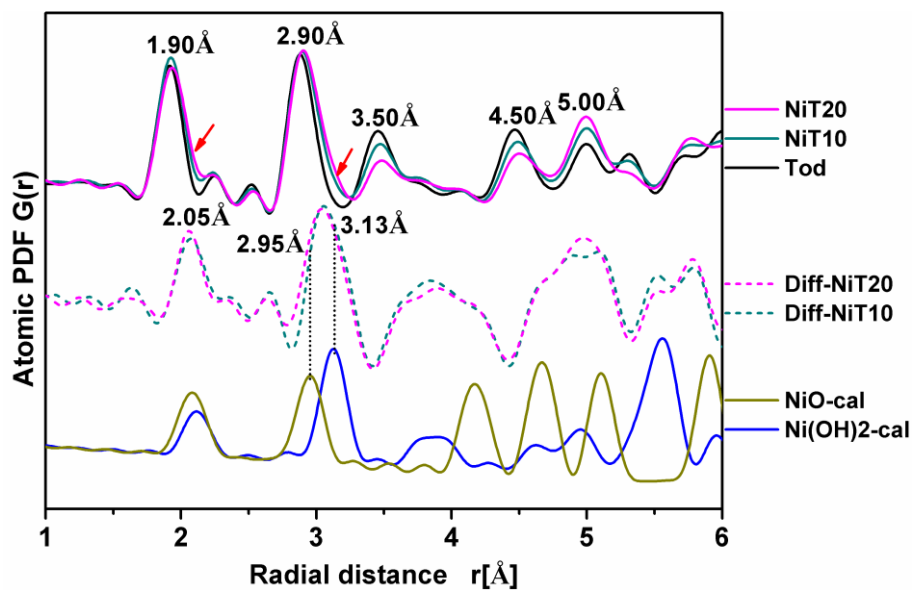
52



53

54 **Fig. 10.** Comparison of Ni K-edge EXAFS spectra obtained for layered precursors
 55 and reflux products with reference spectra. Sample colors as in **Fig. 1.**

56

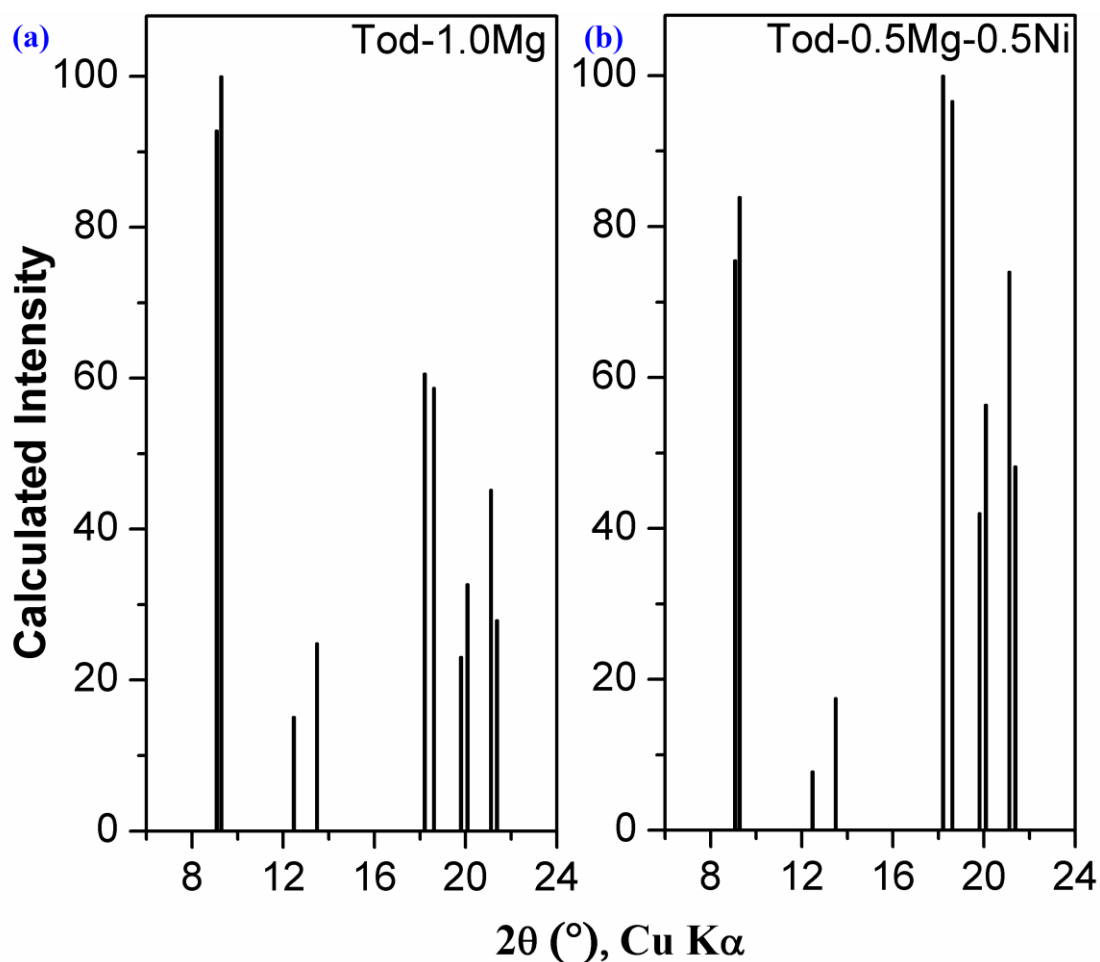


57

58 **Fig. 11.** Pair distribution functions obtained for Ni-rich (NiT10 and NiT20) and

59 Ni-free (Tod) reflux products (top). Middle: d-PDFs relative to Tod PDF data; bottom:
60 PDFs calculated for Ni (hydr)oxides (ICSD #76670 and #28101 for NiO and Ni(OH)₂,
61 respectively). Intensities of experimental PDFs and of difference PDFs were
62 normalized to the 2.9-3.1 Å peak.

63



64

65 **Fig. 12.** Intensity distributions calculated for ideal todorokite (ICDD #38-0475) with
66 (a) only Mg in todorokite tunnels and (b) with Mg and Ni present in a 1:1 ratio in
67 todorokite tunnels. In both cases, the model of Post et al.(2003) was modified
68 assuming the complete filling of the O8 site by H₂O molecules (no cations) and the
69 presence of 1.0 cation (Mg or Mg+Ni) in the Mg site.

70

**Transformation of Ni-containing birnessite to
tectomanganate:
Influence and fate of weakly bound Ni(II) species**

Supplementary material

Geochimica Et Cosmochimica Acta

Zhongkuan Wu^{a,b}, Bruno Lanson^{b,*}, Xionghan Feng^a, Hui Yin^a, Zhangjie Qin^a, Xiaoming Wang^a, Wenfeng Tan^a, Zhongjun Chen^c, Wen Wen^d, Fan Liu^{a,*}

^a Key Laboratory of Arable Land Conservation (Middle and Lower Reaches of Yangtse River) Ministry of Agriculture, College of Resources and Environment, Huazhong Agricultural University, Wuhan 430070, China

^b Univ. Grenoble Alpes, Univ. Savoie Mont Blanc, CNRS, IRD, IFSTTAR, ISTerre, F-38000 Grenoble, France

^c Beijing Synchrotron Radiation Facility, Institute of High Energy Physics, Chinese Academy of Sciences, Beijing 100039, China

^d Shanghai Synchrotron Radiation Facility, Shanghai Advanced Research Institute Chinese Academy of Sciences, Shanghai 201204, China

** Corresponding author: bruno.lanson@univ-grenoble-alpes.fr;
liufan@mail.hzau.edu.cn*

Table S1

Relative proportions of O species in the near-surface of layered precursors and reflux products calculated by fitting XPS O1s data

Sample	O1s (BE)	State	BE(eV)	FWHM(eV)	At. %
Bir	529.35	O ²⁻	529.6	1.59	72.9
		OH ⁻	531.5	1.59	11.6
		H ₂ O	533.4	2.12	15.5
NiB5	529.72	O ²⁻	529.7	1.59	65.9
		OH ⁻	531.2	1.59	18.8
		H ₂ O	532.2	2.12	15.3
NiB10	529.72	O ²⁻	529.5	1.59	60.8
		OH ⁻	531.0	1.59	22.3
		H ₂ O	532.2	2.12	16.9
NiB15	530.06	O ²⁻	529.8	1.59	66.6
		OH ⁻	531.2	1.59	18.5
		H ₂ O	532.3	2.12	15.0
NiB20	530.21	O ²⁻	529.5	1.59	55.6
		OH ⁻	530.9	1.59	25.9
		H ₂ O	532.4	2.12	18.5
Tod	529.89	O ²⁻	529.9	1.59	58.1
		OH ⁻	531.6	1.59	20.9
		H ₂ O	533.0	2.12	21.0
NiT5	529.84	O ²⁻	529.8	1.59	46.7
		OH ⁻	531.4	1.59	29.0
		H ₂ O	532.8	2.12	24.4
NiT10	530.08	O ²⁻	529.8	1.59	47.6
		OH ⁻	531.3	1.59	31.0
		H ₂ O	532.6	2.12	21.5
NiT15	530.15	O ²⁻	529.8	1.59	46.8

		OH ⁻	531.2	1.59	28.9
		H ₂ O	532.5	2.12	23.4
		O ²⁻	529.6	1.59	50.3
NiT20	529.59	OH ⁻	531.0	1.59	29.8
		H ₂ O	532.3	2.12	19.9

Table S2

Relative proportions of NiB and Ni(OH)₂ species obtained from linear combination fitting of NiT K-edge EXAFS spectra using Ni(OH)₂ and corresponding NiB samples as standard references (Fig. S5).

Samples	NiBn /%	Ni(OH) ₂ /%	Error /%
NiT5	82.0	18.0	2.1
NiT10	86.5	13.5	1.0
NiT15	87.1	12.9	0.9
NiT20	85.3	14.7	1.1

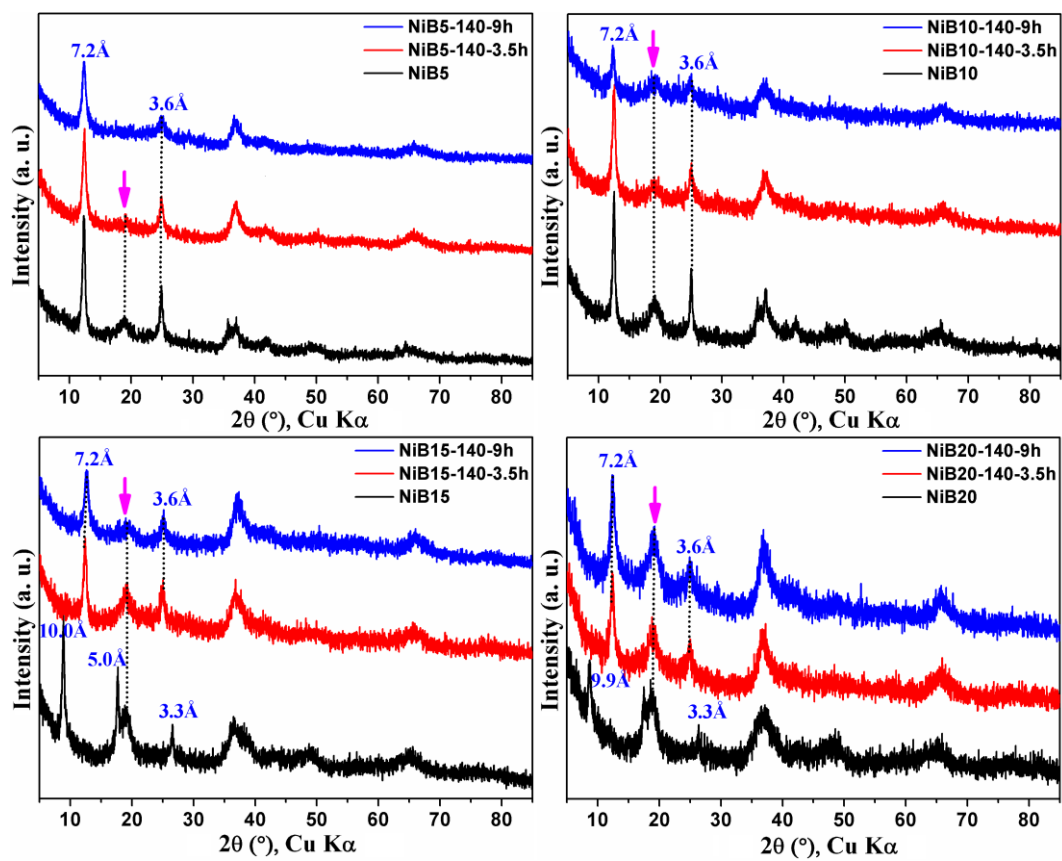


Fig. S1. XRD patterns of fresh layered precursors after heating to 140 °C for different durations

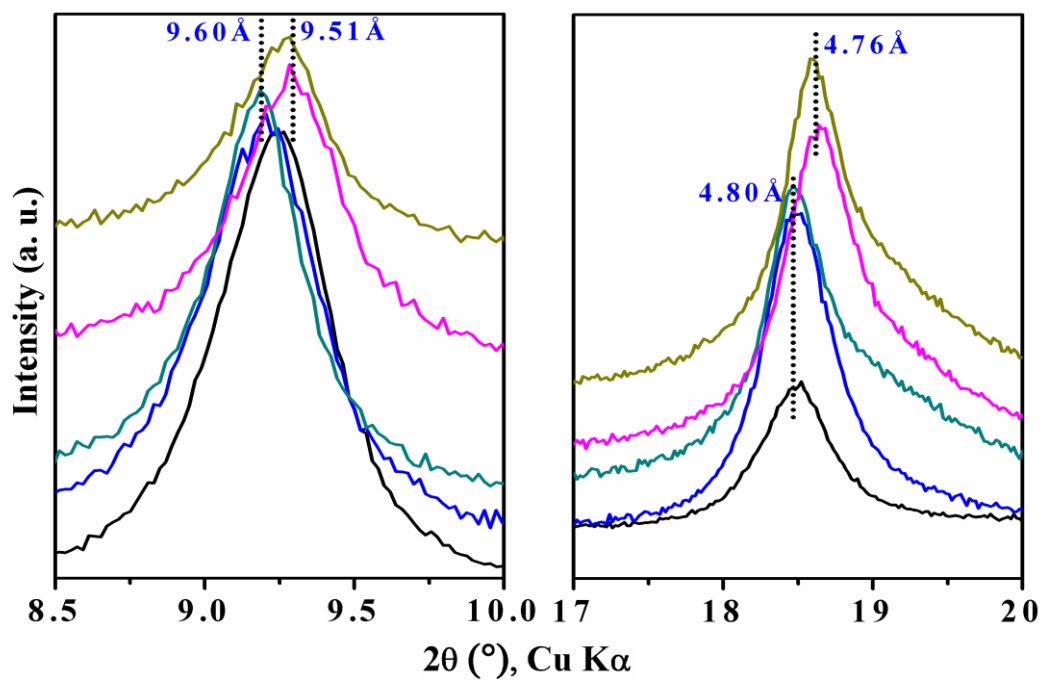


Fig. S2. XRD patterns of reflux products (zoom on low-angle regions). Colors as in Fig. 1.

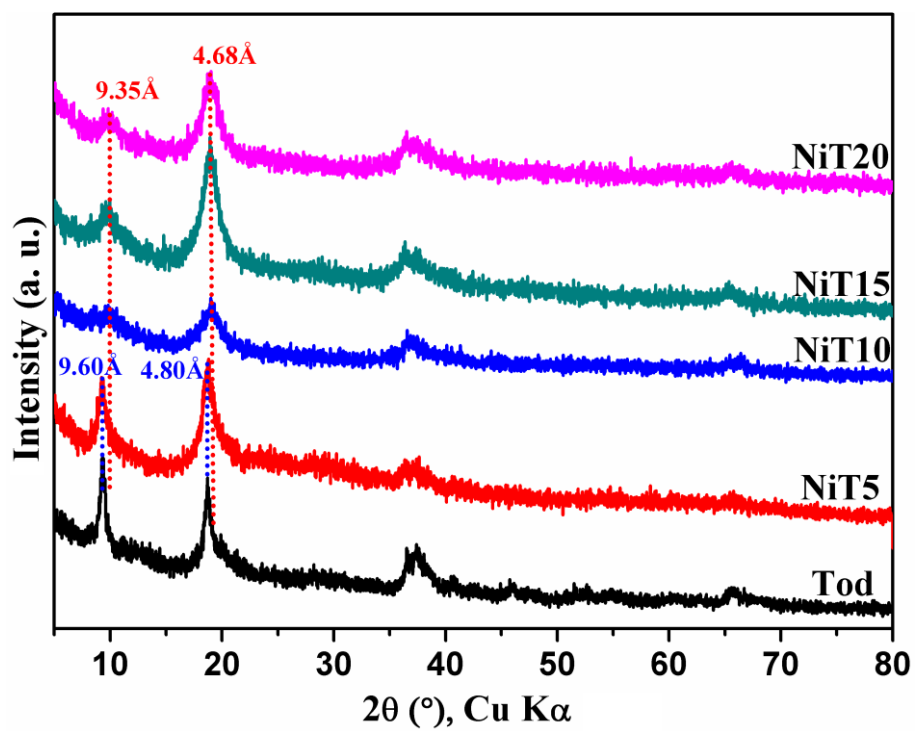


Fig. S3. XRD patterns of reflux products after heating to 140 °C for 12 hours. Colors as in Fig. 1.

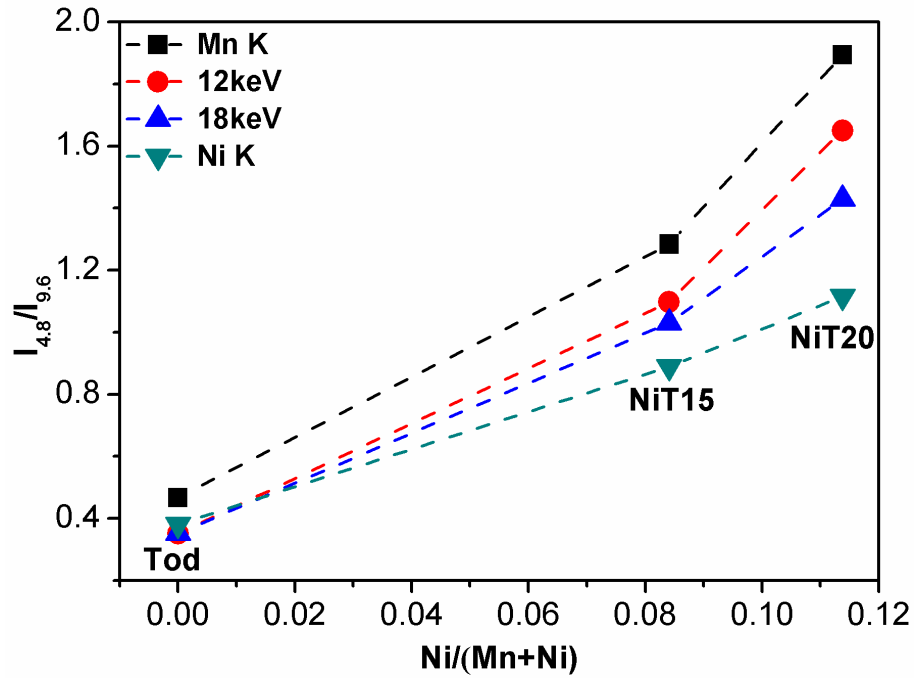


Fig. S4. Intensity ratio of the intensity of 4.8 Å and 9.6 Å peaks ($I_{4.8}/I_{9.6}$) in reflux products as a function of Ni content and X-ray energy (see Fig. 2 for the data).

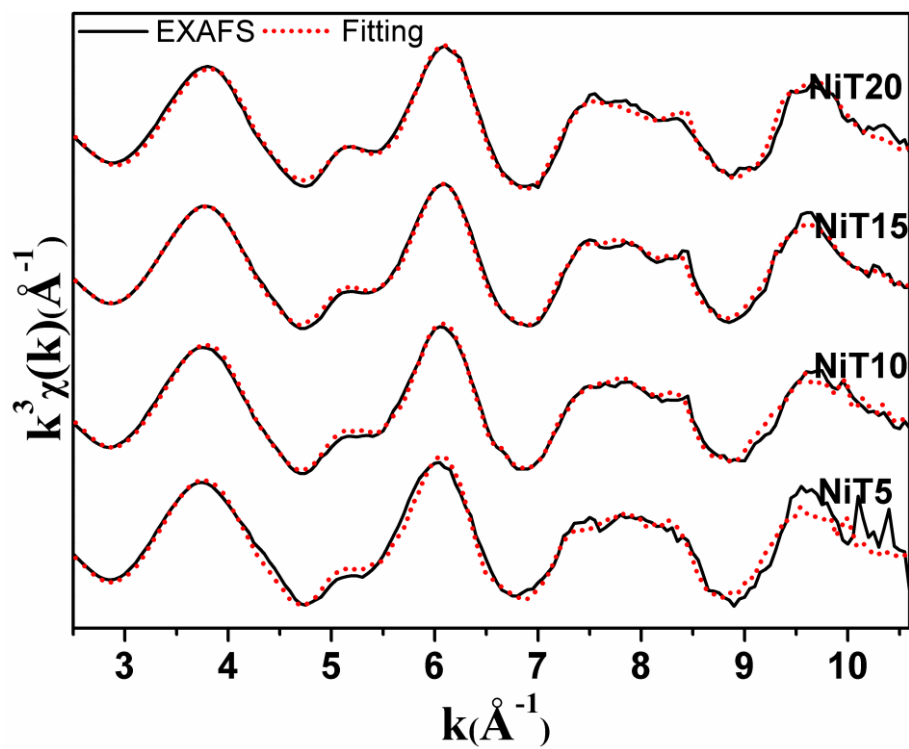


Fig. S5. Linear combination fitting of NiT K-edge EXAFS spectra using $\text{Ni}(\text{OH})_2$ and corresponding NiB samples as standard references.

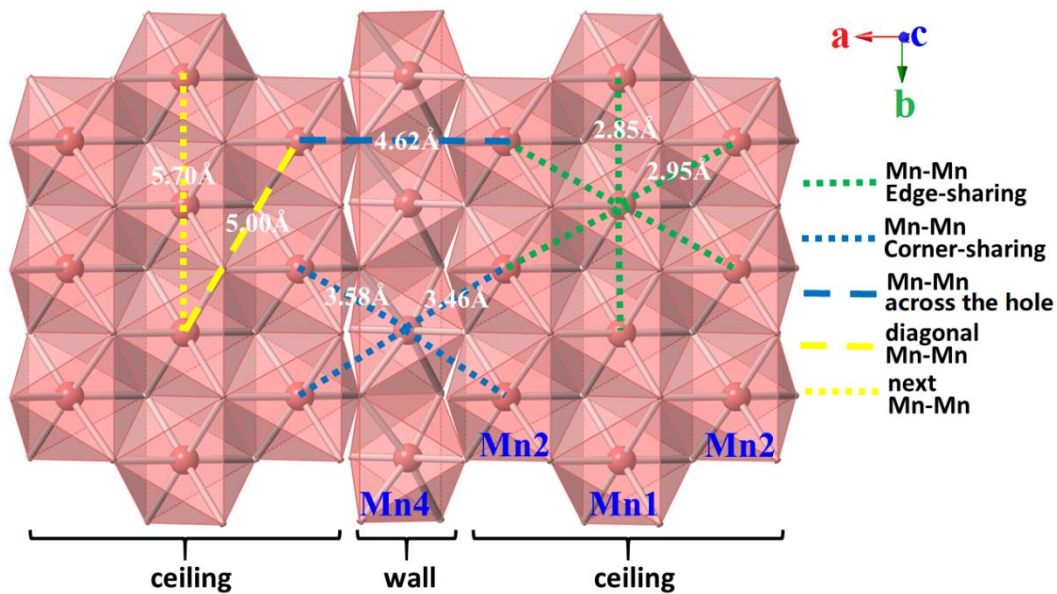


Fig. S6. Interatomic distances calculated for a variety of Mn-Mn pairs and ideal todorokite structure (ICDD #38-0475). The Mn4-Mn4 distance (4.48 Å) which is not reported in the figure is similar to the Mn2-Mn2 distance. Figure modified from Fig. 1(b) in Wu et al. (2019).

REFERENCES

- Wu Z., Peacock C.L., Lanson B., Yin H., Zheng L., Chen Z., Tan W., Qiu G., Liu F. and Feng X. (2019) Transformation of Co-containing birnessite to todorokite: Effect of Co on the transformation and implications for Co mobility. *Geochim. Cosmochim. Acta* **246**, 21-40.